Research Square

Preprints are preliminary reports that have not undergone peer review.
They should not be considered conclusive, used to inform clinical practice,
or referenced by the media as validated information.

Interplay between immune cell damage and depletion, ecological factors and Pinna nobilis Picornavirus (PnPV) infection in the Venice Lagoon (Italy)

Francesca Carella

francesca.carella@unina.it

University of Naples Federico II

Antonia feola

University of Naples Federico II

Grazia Romano

University of Naples Federico II

Serena Aceto

University of Naples Federico II

Jose Rafa Garcia-March

IMEDMAR-UCV Catholic University of Valencia

Jose Tena Medialdea

IMEDMAR-UCV Catholic University of Valencia

Patricia Prado

Institut d'Estudis Professionals Aqüícoles i Ambientals de Catalunya

Giulia Mazzero

University of Naples Federico II

Andrea Sabino

Institute of Marine Science, ISMAR

Marco Sigovini

Institute of Marine Science, ISMAR

Article

Keywords: Pinna nobilis, mass mortality, immunosuppression, RNA viruses

Posted Date: July 1st, 2026

DOI: https://doi.org/10.21203/rs.3.rs-9854708/v1

License: This work is licensed under a Creative Commons Attribution 4.0 International License.
Read Full License

Additional Declarations: No competing interests reported.

Version of Record: A version of this preprint was published at Scientific Reports on October 29th, 2026.
See the published version at https://doi.org/10.1038/s41598-026-77671-7.

Interplay between immune cell damage and depletion, ecological factors and *Pinna nobilis Picornavirus* (*PnPV*) infection in the Venice Lagoon (Italy)

Francesca Carella[1*], Antonia Feola[1,2], Grazia Romano[1], Serena Aceto[1], Jose Rafael Garcia-March[3], Jose Tena-Medialdea[3], Patricia Prado[3,4], Giulia Mazzero[1], Andrea Sabino[5,6], Marco Sigovini[5]

1. Department of Biology, University of Naples Federico II, Naples, Italy
2. Department of Life Sciences, Health and Health Professions, University Link Campus, Rome, Italy
3. IMEDMAR-UCV Catholic University of Valencia, Spain
4. IEPAAC, Institut d'Estudis Professionals Aqüícoles i Ambientals de Catalunya, Carretera del Poblenou, s/n, 43540 La Ràpita, Tarragona, Spain
5. Institute of Marine Sciences - ISMAR, National Research Council - CNR, Venice, Italy
6. Department of Environmental Sciences, Informatics and Statistics, Ca' Foscari University, Venice, Italy

Abstract

We monitored the disease condition of the fan mussel *Pinna nobilis* (L.) in the Venice lagoon (North of Italy) during a period of one and half year (2023-2024) in two areas named Ottagono Alberoni (OA) and Coffa Val Grande (CV). Host and environmental factors (e.g. pen shell age, state of infection, oxygen, temperature, salinity, immune cell depletion with activation of caspase-3) were investigated and shown to influence morbidity and mortality progressiveness in the two areas. During the study period, *Pinna nobilis Picornavirus* (*PnPV*) caused systemic hemic infections in all examined individuals (100%) compromising the organelle compartment of the cells. Ultrastructure revealed widespread viral replication organelles (vROs) occupying most of the host immune cells that arose from a total rearrangement of cytoskeletal membranes that were dedicated to the virus machinery. Our results demonstrate a positive correlation between relative mortality and size classes, showing a higher mortality percentage across all classes, highlighting local differences. Younger, smaller individuals in CV showed higher tolerance and lower mortality rates due to milder viral infections. Conversely, larger adults in OA suffered a 100% mortality rate, leading to the extinction of that population by October 2024. Total Hemocyte Count (THC) was lower in OA (1.77 ± 0.16 and.2 ± 5 x 10^4 cells/ml) compared to CV (1.65 ± 8 x 10^5 - 2.62 x 10^5 cells/ml) and with a positive correlation with viral load, connected with percentage of dead cells

percentage, in turn correlated with animal size, suggesting that number of immune cells is regulated by the level of infection, and also age. Picornaviruses are highly resistant to environmental variables which allow them to persist for long periods in aquatic ecosystems. Viral seasonal presence and interaction with environmental variables need to be clarified.

Keywords: *Pinna nobilis*; mass mortality; immunosuppression; RNA viruses.

Corresponding author: Francesca Carella

e-mail: francesca.carella@unina.it

1. Introduction

Immunosuppressive viruses cause immune system failure. They are responsible for long-term, structural damage, leading to established dysfunction that hijacks immune cells, significantly reducing the body's ability to defend against opportunistic pathogens. [1-2] They are correlated to different disease states, acute and chronic, eventually creating an immune deficiency condition. These types of infections are responsible for changes in cell structure and function.[1-3] The alterations can include cell enlargement, vacuolation, syncytia formation (multinucleated cells), loss of function, cell lysis, and, finally, reduction in cell number.[1,4] In fact, the host response to the infection involves its management through distinct mechanisms, such as the activation of cell death. Apoptosis, a conserved genetic program of cell death (PCD), is critical for organism development and homeostasis but also crucial for cell defense. PCD is executed by a family of cysteine-aspartic proteases known as caspases that assists in regulating the immune response, eliminating self-reactive and infected cells to prevent disease spread.[5-9] Many viral infections in humans and animals have been reported manipulating the apoptotic pathways. However, various features of apoptotic cell death, including maturation of executioner caspase-3, and plasma membrane permeabilization, are commonly shared with other programmed cell death pathways. During the disease the interplay can be complex: some viruses induce apoptosis to facilitate their

spread, while others use it to their benefit, preventing apoptosis to facilitate viral replication and persistence.[10]

In bivalves, several caspases have been identified[11] with homologues to caspase-8[12-13], caspase-2[14], caspase-1[15] and caspase-3. [16-17] Caspase-3 plays the central role of the proteases that cleave cytoplasmic and nuclear substrates allowing cell disassembly. [18-20] So far, the presence of caspase-3 has been demonstrated in oyster hemocytes exposed to cadmium[21] or noradrenaline.[22]

The pen shell *Pinna nobilis* (Linnaeus, 1758), is the largest bivalve of the Mediterranean Sea where it is endemic. Since 2016, the species has been affected by the largest panzootic of marine wildlife in history due to its geographical spread in all the mediterranean countries, reducing the species to few individuals existing in few enclosed bays and lagoons.[23] Recently the species status change from "Vulnerable" category to "Critically Endangered", with a serious extinction risk (Orden TEC/1078/2018). The cause of the mortality, however, has been debated for long due to its multi-pathogen nature involving bacterial and parasite infections[24]. Moreover, factors often associated with outbreaks, such elevated temperatures and salinity, had mixed associations with the MMEs depending on the site, species and data sources.[24-25] In 2021, a Picornavirus affecting pen shell immune cells in most of the residual population of the Mediterranean Sea was reported.[26-28] The virus, named *Pinna nobilis Picornavirus* (*PnPV*) infects the bivalve immune cells, hijacking them to spread, resulting in a two-edged fight of the immune system, pushed between not responding, or responding and facilitating the viral diffusion, damaging cells communications and phagocytosis.[26-28] The virus was reported in 100% of the examined animals in different geographic areas where the pen shell populations still endure: two regions of Spain, Catalonia and Murcia, and two areas in Italy, the Lake of Faro in Sicily and the Venice lagoon.[26,28.]

The Lagoon of Venice (NW Adriatic, Italy), one of the largest coastal transitional ecosystems (CTEs) in the Mediterranean, covering about 550 km of intertidal and subtidal habitats, still hosts one of the last residual populations of *P. nobilis*.[29] The presence of the species is historically documented both in the Venice Lagoon and in the adjacent marine waters since 1792 by the naturalist Giuseppe Olivi in his Zoologia Adriatica[30], and confirmed by subsequent inventories and studies.[30-35] In October 2020, first signs of mortality were reported, reaching 80% in 2023 in the monitored areas.[29] Considering that this population represent one of the last of the Italian waters, the

evaluation of the health status started in 2021 (Carella pers. Comm) assessing the presence of the parasite *Haplosporidium pinnae* and of the *Mycobacterium sherrisi*-like, while the viral infection was reported in May 2023.[24]

Current knowledge of *PnPV* pathogenesis in all the areas of the Mediterranean Sea is still limited. [26-28] Scarce is our understanding of the mechanisms of replication of the virus, the ongoing of the infection over the seasons and the effect on immune cells in affected areas of the Mediterranean Sea. Based on this assumption, in the context of the LIFE PINNARCA project (LIFE20 NAT/ES/001265), we evaluated the presence of the Picornavirus *PnPV* in May and July 2024 in *P. nobilis* in two different sites in the Venice lagoon, Ottagono Alberoni (OA) and Coffa Val Grande (CF). Since other immunosuppressive viruses are known to induce apoptosis and immune cell–mediated elimination and depletion, using a conservative sampling, we provided ultrastructural features of the hemocytes affected by *PnPV* and its effect on animals' immunity, assessing the Total Hemocyte Counts (THC), apoptosis activation using flow cytometry, transmission electron microscopy (TEM) and qPCR for virus detection during Spring and Summer and seasons (2023-2024). Meanwhile, data were collected through field surveys to define population density, mortality, and size structure over some months encompassing the increase in mortality during summer. The data obtained provide valuable information to establish the factors involved in the pathogenesis of mortality in the natural populations, opening new perspectives on the progression of the virus infection in Venice lagoon and mortality event dynamics in the Mediterranean Sea.

2. Results

2.1 *Pinna nobilis* population structure and survival in the Venice lagoon

The sampling areas are reported in **Figure 1**. In OA sub-plots (374.3 m^2 overall), a total number of 428 individuals (116 alive) were counted in March 2023, with 120 (22 alive), 153 (47 alive), and 155 (47 alive) recorded in replicates A, B, and C, respectively. The mean overall density of the study area is 1.14 ind. m^{-2} (st. dev. = 0.092). In CV area sub-plots (324.2 m^2), 128 individuals (38

alive) were recorded in March 2024, with 36 (15 alive), 37 (10 alive), and 55 (13 alive) in replicates A, B, and C, respectively. The mean density is 0.4 ind. m^{-2} (st. dev. = 0.128). No shell was observed to be displaced after death. No recruitment of juveniles was recorded in either study area during the survey period. The temporal trend in survival rates, expressed as the live-to-total ratio, is shown in **Fig. 2**. February 2024 values for CV local population were estimated by considering alive at that moment the dead individuals recorded in May characterized by intact shell. Overall, survival rates showed a progressive decline across both areas and all the sub-plots during the study period. Mortality in both years began to be observed in May, and intensified in the following months, with peak mortality rates recorded during the summer period, between July and September.

Regarding the OA local population, the mean live-to-total ratio decreased from 0.26 in March 2023 to 0.019 in November 2023. This led to a substantial reduction in mean density, from 0.31 down to 0.023 ind. m^{-2}. By October 2024, values further declined to 0.0078 ind. m^{-2}. In the CV local population, although the available data are limited to 2024, live-to-total ratio values are overall higher, with mean values decreasing from 0.32 in February to 0.25 in October, respectively. The mean mortality rate appears slightly higher than in OA during the same period, however, comparisons are difficult due to the very low number of specimens still alive in OA in 2024. The density decreased from 0.12 ind. m^{-2} in February 2024 to 0.096 ind. m^{-2} in October.

The overall size distribution (both live and dead individuals) for both areas as of February 2024 is shown in **Fig. 3A**. The histograms are skewed towards larger size classes, corresponding to adult specimens. In OA, the mean and median sizes were 44.73 cm and 44.87 cm, respectively (IQR: 40.15–49.69 cm). In contrast, CV exhibited lower average values, with a mean of 39.32 cm and a median of 38.60 cm (IQR: 34.02–43.29 cm). In **Fig. 3B** the size distribution of live individuals are compared at different moments, in March 2023 (only for OA), February and October 2024 (for both OA and CV). The distribution of residual OA specimens in February 2024 appears shifted towards smaller size individuals. Relative mortality calculated for 10-cm size classes over an eight-month span (encompassing the summer mortality peaks) for 2023 (OA) and 2024 (OA and CV) is presented in **Fig. 3C**. A simple linear model ($Y = b_0 + b_1X$) was fitted to both 2023 OA dataset and 2024 CV dataset (for the latter, the value corresponding to the largest size class was excluded, as

it was based on a single individual). The linear regression for the 2023 OA dataset was statistically significant (adjusted $R^2 = 0.728$, $p = 0.0418$), yielding the following estimates: $b_0 = 0.62$ and $b_1 = 0.0078$. The regression for the 2024 CV dataset was also statistically significant (adjusted $R^2 = 1$, $p = 8.3 \times 10^{-17}$), with parameter estimates $b_0 = -0.36$ and $b_1 = 0.014$. Overall, both models indicate a positive relationship between size and mortality, with similar slopes, although they differ substantially in their intercepts. In addition, a Generalized Linear Model (GLM) with a quasibinomial distribution and logit link function was fitted to both complete datasets. For the 2023 OA dataset, the GLM revealed a highly significant positive effect of size on mortality rates ($\beta = 0.139$, $p < 0.01$), accompanied by a strong reduction in deviance (from a null deviance of 0.871 to a residual deviance of 0.026). For the 2024 CV dataset, the GLM showed a similar positive trend ($\beta = 0.265$), however, the effect was not statistically significant ($p = 0.14$), likely due to the limited number of size classes. Nevertheless, a reduction in deviance was still observed (from 3.19 to 0.39). No model was fitted to the 2024 OA dataset due to the very small sample size.

2.2 Environmental characterization

Over the 18-month time series, water temperature at OA ranged from 6.7 to 32.3 °C (monthly variability Suppl. **Fig. 1A**), while daily salinity varied between 25.9 and 38.3 (mean: 33.1; median: 33.6; monthly variability **Suppl. Fig. 1B**). During the shorter deployment at CV, temperature and salinity ranges were 8.9-32.9 °C and 29.3-34.2, respectively. Dissolved oxygen (DO) at OA ranged between 0 and 17.01 mg L^{-1} (mean: 7.63 mg L^{-1}; median: 8.38 mg L^{-1}), whereas in CV between 0 and 15.77 mg L^{-1} (mean: 8.03 mg L^{-1}; median: 8.17 mg L^{-1}). The DO time series at OA is incomplete from 28 July to 20 September 2024 due to sensor malfunction. Despite the different deployment lengths, temperature trend appeared comparable across both sites during the overlapping period. A robust comparison of salinity between the two sites is precluded by the limited data overlap, also due to sensor malfunctions. DO was the sole parameter to exhibit clear differences between the two study areas. During summer, OA study area experienced more frequent, intense and prolonged hypoxic events (DO < 2.0 mg L^{-1}) compared to CV. Anoxic conditions (DO < 1.0 mg L^{-1}) were restricted to OA during late June and July. Prolonged hypoxic events typically occur

during neap tides. In contrast, CV exhibited only short-term hypoxia, primarily in July and August, with sporadic episodes extending into October and November (**Suppl. Fig. 1C**).

2.3 Immune cells morphology in the two areas

Observation of semithin sections of *P. nobilis* hemocytes showed a different situation in May and July 2024 and in two areas. In May, in OA, hemocytes displayed an extensive number of apoptotic cells with no nucleus and apoptotic bodies. In July, in the same area, hemocytes displayed additional long projections and higher number of dead cells (**Fig 4A-B**). Cells showed many alterations such as long and numerous filopodia and blebs formations (**Fig. 4C-E**). In CV the number of apoptotic bodies was lower and projections less evident. In both areas, cells were mostly basophilic at MMG stain, displaying numerous vacuoles, and showing granules/dots (**Fig. 4F-L**).

2.4 Total Hemocyte Count (THC), caspase 3 activation and pathogen infection

The mean number of circulating hemocytes was 1.77 ± 0.16 x 10^5 cells/ml in OA in May and 9.2 ± 5 x 10^4 cells/ml in July. In CV, the values were 1.65 ± 8 x 10^5 cells/ml in May and 2.62 x 10^5 cells/ml. In OA, in May 2024, number of dead cells ranged from 27 to 63% (mean value: 40,5) and active caspase 3 ranged from 0 to 5.68%. In July, number of dead cells increased, from 32 to 70% (mean value: 50,14), and active caspase 3 passed from 0 to 66.6% (**Fig.5A**). In CV in May 2024, it ranged from 12-32% (mean value:25,6) and active caspase 3 from 0 to 36.7%. In July, number of dead cells ranged from 39 to 54% (mean value: 47,3), and active caspase 3 from 0 to 75.0% (**Fig.5B**).
The quantitative real-time PCR experiments conducted on the *cDNA* of *P. nobilis* hemocytes collected in different sampling points in Venice lagoon gave positive results for the primer pair designed on the reconstructed sequence DN35348_DN58105, similar to a *Chaetoceros tenuissimus* RNA virus type II. Viral RNA was detected in all the other samples examined with variable infection levels in both the areas (**Fig.5C**). The THC status showed a positive correlation with logNRQ value ($P < 0.0022$, r = 0.62) and positive correlation of logNRQ value with animal size

(*P < 0.626*, r = 0.62), suggesting that number of immune cells is regulated by the level of infection also related with animal size (**Fig.5D-E**).

Realtime PCR for *PnPV* conducted on mantle tissues in February 2024 in 5 out of 8 (62.5%) gave positive results. The samples of mantle taken in the individual Pn5Old_OJ24M resulted also positive. End-point PCR on hemocytes performed for *H. pinnae* and *Mycobacterium* sp. resulted both negative.

2.5 Ultrastructural features of *Pinna nobilis Picornavirus* infecting cells

As previous descriptions from Carella et al.[26] and Iaria et al.[28], in both OA and CV, the Pen shell hemocytes ultrastructure revealed the features of *PnPV* infection at different phase of development in all animals (100 %). Alterations of cytosolic organelles were variable depending on the virus phase of development, showing viral Replication Organelles (vROs) of different dimensions. The schematic of the changes observed is represented in **Fig 6**.

The cells could appear more elongated or rounded, filled with complex Double Membrane Vesicles (DMVs) forming virions. They could also display prominent presence of filopodia at the level of plasma membrane or be stellated with filopodia projections (multipolar) or binucleated (showing syncytium) (**Fig. 7A-E**). The population of cells could also be represented by dead bodies with no nucleus and residual DMVs, as reported by cytology (**Fig. 7F**). This situation was more evident in July in both areas.

Filopodia presence and microvilli were a common feature of the infected cells in both seasons and areas. They were variable in number for each cell, ranging from one to 5-7 also accompanied by other types of actin rearrangement, such as the presence of smaller buds and microvilli (**Fig. 8**). The filopodia averaged 7.4 ±05 µm in length (n = 59) or could be significantly shorter (average length, 2.37±08 µm; n = 60). These membrane projections were more visible when cells were highly damaged, showing total loss of cytoskeleton and an increased size, fitting with the activation of apoptotic pathway. In those cases, unassembled amorphic viral substance was concentrated at the periphery of the cells in contiguity to the cell membrane and expanding to the filopodia/microvilli, associated with viral particles in formation or mature (**Fig.8A-B**). The

filopodia were seen as bridges between cells with visible actin filaments and passage of viral particles in May and July in OA (**Fig. 8C-E**). Formation of budding and numerous viral particles carrying vesicles were also visible (**Fig. 8F**). Individual Pn3CVM24/Pn3old_CVJ24 showed 58% of dead cells in both the seasons while the value reached 76% for the individual Pn5_OA24.

Replication organelles (ROs) were represented by a total rearrangement of cytoskeletal proteins and organelles membrane structures, creating an independent compartment to facilitate viral genome replication **(Fig. 9)**. In the cells, they appeared in all the cells as a complex system made of membrane vesicles of different dimensions. The ROs seemed to originate by a remodeled ER and nuclear membrane structure, and interacting with the Golgi complex intermediate compartment (**Fig.9A-E**). The transformed ER comprised flattened sacs (cisternae) connected to the nuclear envelope as well as loose interconnected membrane tubes and sheets and visible ribosomes (**Fig.9A-C**). Viral budding at the endoplasmic reticulum (ER), ER-Golgi-Intermediate Compartment and Golgi apparatus was visible, was also the site of replication of the viral particles (**Fig. 9D-E**) in some case passing from a rosette-like structure assembling with a common stalk form the vesicles or Golgi modified structure to a mature single viral particle (**Fig. 9F-G**). In all the seasons and areas, cells might also display the presence of *PnPv* repeatedly surrounding the nucleus, interacting with the nuclear membrane and actively entering the nuclear compartment, with visible viral particles present among chromatin fibers.

2.6 Flow cytometry and active Caspase-3 in *P. nobilis* hemocytes in Venice lagoon

Flow cytometry analysis detected different sub-populations in *P. nobilis* hemocytes based on size and internal complexity and/or granularity (**Fig. 10A**). The type 1 was the most abundant circulating hemocyte (~50% of circulating cells) with a medium size and medium internal complexity and granules, previously described in *P. nobilis* as granulocytes[27]; the type 2 had the smallest size and the lowest complexity, representing the hyalinocytes (10-20%); type 3 was the one displaying the same size of the type 1 but the highest internal complexity and granularity, variable in percentage and depending on the individual (8-12%). Moreover, we observed a fourth sub-population not reported previously, named type 4, that has bigger size and greater

complexity when compared to the others (0,5-15%). When comparing cell types and activation of Caspase-3, type 4 sub-population corresponds to those in which Caspase-3 is activated (**Fig. 10A-B**). Furthermore, another sub-population was present only in few animals, smaller and poorly granulated, and on the bases of propidium iodide (PI) staining it was not nucleated, as it did not absorb PI, and it was named type 5 (**Fig. 11**). In **Tab. 2**, for each type of cell, the percentage of cells in which Caspase-3 activated is reported in association with the percentage of cell numbers compared to total events acquired.

Percentage of each population of cells was variable depending on individuals, season and areas (**Sup. Tab. 1**). Even if the type 1 is the most representative sub-population, an increase in percentage of type 2 was observed in certain individuals in both sites and seasons (animals Pn3OAM24 and Pn1oldCVJ24). Moreover, in July, the hemocytes showed a higher Caspase-3 activation than in May, independent from the site. Morphologically, when Caspase-3 is activated, it appears in a sub-population bigger and more complex than the other one, here called type 4, except for the two individuals Pn1New_CVJ24 and Pn1New_CVJ24. This can be due to cell transformation and biochemical events can occur in different moments.

In some case, animals showed distintive features over seasons and areas. In OA in May many cells were positive to PI staining, but negative to caspase-3, while in July nucleated cell accounted only the 5%, and about 43% of them were death, as for the animal Pn5_OA24 (**Fig. 11**). Instead the animal Pn3CVM24 the number of cells was low and the cell populations didn't have activate caspase-3. In July there was an increased count, a reasonable number of cells can be observed in each subpopulation, with a 75% of active caspase-3 (**Fig 12).** This is in accordance with the situation observed at ultrastructure where numerous dead cells where observed.

2.7 Virus phylogeny

The NJ tree based on the 193 bp *PnPv* fragments obtained in this study revealed a statistically well-supported clade (96% bootstrap support) including all sequences from the Venice and Sicily, together with the sequence from Spain (accession number OR448788) reported in the previous study (Carella et al., 2023b). This clade is closely related to the *Chaetoceros tenuissimus* RNA virus type II (**Fig. 13**).

3. Discussion

In this study, we investigated the complex host-virus interactions associated with different environmental parameters involved in the disease affecting *Pinna nobilis* in the Venice Lagoon. We report the persistence of *PnPV* in the Venice population in 2024, following its initial detection in 2023, providing new insights into population structure, environmental factors, immunopathogenesis, and virus phylogeny.

The *PnPV* is an RNA single strand virus previously reported in Spain (Catalonia and Murcia region), in Italy, in Venice lagoon in 2023[24] and in the Lake of Faro population (Siciliy) in 2024.[28] The virus is a Sogarnavirus, a picornavirus originally identified in the marine diatom *Chaetoceros tenuissimus* (designated as C*. tenuissimus RNA virus type II*). The amplified region was identical to the strains found in populations from Spain and Sicily; only two sequences showed slight differences in a few base pairs.

Ecological factors, population structure and pathological threats

In 2024 the local populations of *P. nobilis* were characterized in terms of densities, size structure and mortality in both OA and CV study areas. The monitoring of the OA study area was initiated in 2020, coinciding with the onset of the Mass Mortality Events (MMEs) in the Lagoon of Venice.[29] Before the pandemic, the OA area initially showed a high density of live individuals, estimated at 0.8 ind./m². The CV study area, located at a relatively short distance (~3 km) from OA, hosts the highest known density of live *P. nobilis* in the Venice Lagoon at present. Although the available data do not allow for a precise determination of the cohort structure, individuals in the present study probably fall in the range from 2 to over 10 years old.[37] In both study areas, the population size-frequency distribution is skewed towards larger size classes, a pattern widely documented for this species.[38-39] This pattern has been associated to biological traits such as high longevity and a significant growth slowdown after maturity as well as higher mortality rates in young stages, generally attributed to intense predation.[25,40-42] In our study sites, the overall size-frequency distributions and the variable degree of shell degradation suggest the co-presence of multiple cohorts and an older settlement in OA compared to CV. However, the observed shifts in size-frequency distributions over time suggest a higher mortality rate for larger size classes, although

the total proportion of dead individuals varied between the study areas. Our results demonstrate a positive correlation between relative mortality and large size classes, and therefore age. Due to data availability, the direct comparison between sites was limited to the 2023 dataset for OA and the 2024 dataset for CV. Although both datasets exhibited a similar linear trend, they differed in their intercepts, with OA showing a higher relative mortality across all size classes, highlighting local differences. Our findings suggest a higher vulnerability of older individuals to the ongoing epidemic, which is consistent with prior observations in other Mediterranean regions.[25,43] This may be driven by several physiological and pathological factors. A distinct peak of mortality is observed during the summer months, with the maximum mortality rate recorded between July and September 2023, and from May to July 2024 across both areas. The peak of summer mortality is also consistent with our results on the status of the immune system of the population as demonstrated by THC, flow cytometry and electron microscopy.

In the Venice Lagoon, temporal variability was observed among sites for temperature, salinity, and dissolved oxygen. Those parameters are correlated with animal physiology but also to pathogens distribution and activity, as previously reported by other authors.[25,42] The mortality trend is characterized by a synchronous seasonality in both sites, which points to seasonal variation in key environmental variables, in particular water temperature, whose variation over time appears similar in the two areas.

Water temperature is considered a typical initiating factor for the mortality across Spain, France, and Italy.[24,42] Temperature is a key stress factor involved in shellfish summer mortality, by causing metabolic stress, lower dissolved oxygen availability, and increased pathogen susceptibility.[25,44] Typically, the onset of mortality has been associated with temperature exceeding 13.5 °C.[45] Temperature was recorded in OA starting on 31/05/2023, just after the May monitoring. The mean value of the first two weeks of June was 23.82°C (range between 21.31°C – 27.41°C). In 2024 instead, the mean T value in May is 20.28°C (range between 16.31°C – 24.41°C) in OA study area. Water temperature data are available in CV area only since June 2024, nevertheless in the overlapping period with OA measurements they follow closely each other.

Dissolved oxygen (DO) is an important parameter that affects the biology, physiology, and immunology of aquatic animals. In general, hypoxia negatively impacts the food consumption rate and assimilation efficiency, as well as increasing respiration rates in many bivalves.[46-47] As a result, it reduces the energy allocation for bivalve growth, shell formation, and reproduction. The tolerance of bivalves to hypoxia largely depends on size and species, with larger bivalves being more susceptible to hypoxia and intertidal species being relatively more tolerant.[47]

At CV, the DO concentration was relatively stable, with only a few shorter hypoxic events concentrated in late summer and autumn. Instead, in mid-July 2024, the probe at OA highlighted severe nocturnal anoxic (DO < 1.0 mg L-1) and hypoxic (DO < 2.0 mg L-1) events during neap tides. Since the sensor was located within 20 cm of the seabed and outside the *Cymodocea* meadow, these values likely reflect micro-habitat conditions confined beneath macroalgal mats, where organic matter decomposition triggers intense oxygen depletion. However, the site proximity to the Malamocco tidal inlet ensures significant hydrodynamics and oxygenation in the upper water column. Large adult individuals can protrude significantly above the sediment and have access to better-oxygenated layers, thereby mitigating respiratory stress. Conversely, smaller juveniles are more prone to these conditions, particularly when located outside well-oxygenated seagrass meadows. Yet experimental studies have confirmed that juveniles of the species are relatively resistant to moderate exposure to hypoxia[48], and the continued existence of dense populations in highly variable lagoonal habitats underscores their potential for physiological plasticity and resilience in these suboptimal environments.[25,49]

Salinity is another important parameter to ponder. Mortality events have been predominantly associated with a salinity range between 36.5 and 39.7 PSU.[25] Environmental conditions outside this window, typically found in coastal transitional ecosystems, can act as a protective barrier. The nature of these refugia differs based on their hydrological regime. In the Ebro Delta, particularly in Fangar Bay, the spread of the parasite *H. pinnae* was hindered by low salinity values (30.5–33.5 PSU).[25] Conversely, the Mar Menor lagoon typically provides protection through its hypersaline conditions (ranging from 42 to 47 PSU).[50] During the data overlap period, the two stations exhibited a highly synchronized temporal trend, sharing very close overall values with a mean salinity of 33.09 at CV and 32.41 at OA. Although the long-term salinity offset between the two

sites was only 0.68 units, the associated SD = 0.99 indicates minor localized fluctuations. In our study, samples analyzed during this period showed no presence of *H. pinnae*.

Immune status, animal infection and ecological factors

Total hemocyte count (THC) is a critical indicator of bivalve's immune condition. This parameter changes dramatically during infection, with severe or prolonged infection leading to a significant reduction in circulating immune cells, reported as heamocytopenia.[51] In our study the population in the two areas revealed a different level of infection and THC values over the seasons, also lower when compared with many other bivalve species[52-53] and previous studies on *P. nobilis.*[54] In fact, in previous findings before the MMEs on the pen shell the amount of circulating hemocytes corresponded to 5×10^5 cells, a much higher number if compared with the recent situation of residual wild populations, where recorded values ranged between 7.9 ± 0.3 cells $\times 10^4$ –2.30 ± 1.0 cells $\times 10^5$ in 2021-2022 in Ebro Delta and Murcia[24,26] and $9.2 \pm 5 \times 10^4$ -2.62 x cells 10^5 in this study (2023-2024). THC values were correlated with *PnPV* infection level and animals' size. THC values in OA were lower when compared to CV, demonstrating and higher capability of animals from CV to cope with the infection after damage.

The loss of immune cells is itself a cell death mechanism activated which bring to immunodeficiency.[55] For this reason, here we evaluated the immune cells death percentage in each individual along seasons analyzing caspase-3. Over 2024, in OA the mean percentage of dead immune cells was around 40,5- 50,14 while in CV it ranged from 25,6 to 47,3, with an increased value in summer in both areas. Moreover, flow cytometry showed the major damage to the immune cells and activation of the executioner caspase-3 in both sites in Summer 2024. At the same time, we recorded a higher viral load in July 2024 in OA and slightly higher, but steady in CV. The activation of caspase-3 in turn cleaves key proteins, causing cytoskeleton collapse, DNA fragmentation, and apoptotic body formation, ultimately sacrificing the infected cell to contain the spread of the pathogen. Furthermore, has been demonstrated that high temperatures (e.g., 30-33°C) can significantly increase CAS-3 mRNA levels, indicating also that stress-driven apoptosis is part of the mortality syndrome in summer.[17] When considering the correlation of the viral load

and animals' size, smaller individuals in CV showed lower level of *PnPV* infection. This could be due to lower filtration activity and consequent inferior viral particle accumulation over time, a less compromised immune system due to the younger age/size.

About the *PnPV* infection and seasonality in the environment, we don't have any information on its distribution. Marine viruses exhibit strong seasonal dynamics, with abundance peaking in Spring and nutrient-rich summer months (often 2.0×10^7 viruses/mL), corresponding with increased bacterial and phytoplankton production. In our case, we have scarce information about the life cycle of this Picornavirus outside of the host and the effect of abiotic factors on viral replication, presence and potential vectors. Yet, we know from literature that the most similar virus, *Chaetoceros tenuissimus picornavirus*, show strong seasonality linked to phytoplankton population blooms, typically peaking during summer to autumn (July to September) in coastal Japanese waters.[56] Picornaviruses are highly resilient naked (non-enveloped) viruses that can persist in the environment for extended periods. Because they lack a fragile lipid envelope, they are resistant to pollutants and extreme pH levels including acidic conditions.[57-59] They can persist for long periods on surfaces and in water and low oxygen conditions as they do not metabolize and therefore do not require oxygen for survival or replication.[58-59]

Immune cell types and damage related to ultrastructural details

Based on flow cytometry, this study discriminated against immune cell types during infection by their size and internal complexity, consistent with previous reports on this viral infection.[26] In contrast to the situation observed in Spain, we identified four types of hemocytes: hyalinocytes, granulocytes, a third type (type 3) characterized by larger size and high internal complexity/granularity, and a fourth type (type 4) that was even larger and more complex. From a functional perspective, our data suggests that type 4 may be a morphological variant of type 1 (granulocytes), larger and more granular cells found in animals undergoing an active immune response in the final stages of apoptosis. From previous observations these cells corresponded at ultrastructure to hemocytes with advanced replicating phases of *PnPV* infection, displaying numerous and complex vRO containing Double Membrane Vesicles (DMVs) and having multipolar/stellate shape with formation of long filopodia. The presence of bigger vRO might

primarily be due to higher viral capability in assembling and scaffolding nonstructural protein in the cells. This could reflect more permissible behavior to the infection of the pen shell immune system of Venice population, and lower resistance to the disease.

Caspase-3 is activated via intrinsic (mitochondrial) or extrinsic (death receptor) pathways, leading to characteristic ultrastructural changes in immune cells. Its activation involves proteolytic cleavage of pro-caspase-3 into active p17 and p12 subunits.[60] Using ultrastructure, we demonstrated that viral-infected immune cells exhibited rearranged cytoskeleton and organelle damage. The *PnPV*, like other positive stranded RNA viruses investigated to date, replicates its RNA in association with organelles inducing enormous spatial reorganization of the cytoplasm to create a network of vROs in the perinuclear region along with fragmented and stacked membranes of the Golgi apparatus. Mitochondria was the organelle that was observed intact in the cell most of the time, while the virus was replicating. In advanced phases of damaged cells, broken cristae were observed. We can hypothesize that at this point mitochondrial outer membrane permeabilization releases the cytochrome c that trigger caspase activation (caspase-9/3).

For the first time, we observed that hemocytes infected by *PnPV* displayed filopodia formation with active passage of viral particles. Communication between two or more neighboring cells was evident, finding filopodial bridges (filopodia joined but not fused). Filopodia are actin-rich plasma membrane protrusions elicited to enhance infectivity in the entry step into various kinds of cells and reported in SARS-CoV-2, Rous sarcoma virus (RSV), Herpes simplex virus type 1 (HSV-1) among the others.[61-62] Generally, the first step of every viral infection involves virions engaging the cell surface, with subsequent penetration of the cell membrane and entry into the cytoplasm. The physical barrier imposed by the actin network must be weakened, a process involving the stimulation of actin cytoskeleton remodeling. Virion binding can initiate signaling events that change the cell surface and activate endocytosis. Evidence for the endocytosis of infecting virions is widespread and is often actin dependent or actin stimulated by clathrin-coated pit-mediated endocytosis.[63] Virus entrance could be regulated by heparan sulfate proteoglycans (HSPG) which are expressed on the membrane of the target cell, called the attachment step, as we observed in

our study. HSV then surf along the surface of these filopodia by using their glycoprotein gB attachment to HSPG causes actin remodeling.

4. Conclusions

Our study confirms the presence and effects of *PnPV* in another Mediterranean population. These results help identifying survival areas for the species, highlighting distinct population conditions locally within the same lagoon system. Furthermore, we begin to disentangle the complex interaction between population structure, environment, tolerance thresholds and infection dynamics. Site-specific factors and pen shell demography emerged as two key players in immunity and disease during infection. Additionally, this study advances our understanding of how immunity functions in natural populations, raising questions about Picornavirus infection, and provides urgently needed information on the conditions that influence disease in an ecologically important host species. Our findings could indicate that the infection has compromised the resilience of younger individuals, historically endured high temperatures and hypoxia, leading now to reduced survival rates. Using our ultrastructural dataset as a foundation, we can begin to design studies aimed at answering these questions that will provide useful insights into *PnPV* pathogenesis. For instance, the biogenesis of vROs is still poorly characterized, and we do not have detailed information on the host or viral factors that contribute to their formation. Identification of these features can help in comparing pathogenesis in different areas and population.

Picornavirus can infect a vast range of aquatic life. They are widely distributed across the oceans and are major drivers of marine ecology and biogeochemical cycles. Indeed, they act as key mortality agents in aquatic ecosystems, controlling population blooms and altering marine biogeochemistry. *Chaetoceros tenuissimus RNA virus* specifically infects phytoplankton and microalgae. When lyses algal cells, it terminates massive oceanic blooms, releasing amounts of dissolved organic matter (DOM). The presence of non-enveloped, proteinaceous capsid renders picornaviruses highly resistant to environmental stressors—including UV radiation, salinity and oxygen changes, and general physicochemical degradation—which allows them to persist for long periods in marine and aquatic ecosystems. The occurrence of free viral particles in the

environment and their transport via phytoplankton vectors warrants further investigation. Genome characterization of *PnPV* in Venice lagoon and the other areas is also needed.

The existence of this virus is largely underestimated by the scientific community because it is difficult to diagnose, due to its tropism and its nature as an RNA virus. Mantle biopsies have demonstrated to be effective in some cases but might depend on viral particle presence in the water captured but mantle cilia, as reported in other marine viruses. New detection methods in animals are currently under development to simplify the diagnostic process. At the same time, e-RNA based monitoring can be used to identify potential transmission sites.

5. Material and methods

5.1 Study area

In the context of LIFE PINNARCA and LIFE PINNACARE Projects a study to evaluate health status of the Venice lagoon population and with different diagnostic purposes was performed between October 2021 to July 2024. In 2023 the activities focused on the area of Ottagono Alberoni (OA)[24] and after, in 2024, also on a second area named Coffa Val Grande (CV), chosen because of the presence of significant densities of live specimens, as well as recorded mortality episodes. Both OA and CV are located in the southern part of the Lagoon, in the Malamocco sub-basin, and fall into the marine tidal delta hydrogeological zone[64], characterized by euryhaline conditions (salinity > 30 ppt) and high-water exchange (**Fig. 1**). Ottagono Alberoni is a sheltered island near the Malamocco inlet. The depth range of this area is between -1 m and -1.5 m with reference to mean sea level. The sandy silt substrate is characterized by the presence of seagrass meadows of *Cymodocea nodosa*, with canopy cover varying according to the season (minimum values in winter), and macroalgal cover. Coffa Val Grande is an area located along the Val Grande channel, which branches off from the main waterway Canale dei Petroli, the latter originating at the Malamocco inlet. The area features a monitoring station managed by the Venice Water Authority (**Fig. 1**). The bathymetry range is 1.5 – 2 m below the mean sea level. Also in this area, the surficial

sediments grain size is sandy silt, and the seabed cover is characterized mostly by *Cymodocea nodosa* meadows.

5.2 Population structure and survival

Size structure and mortality of local *P. nobilis* populations were analyzed in both the OA and CV study areas. Due to the species' high densities, for each study area the analyses were concentrated on three roughly equidistant plots of about 120 m^2 (20 x 6 m) within homogeneous habitat patches of approximately one hectare. This design was chosen to ensure the capture of local population variability while maintaining a sustainable sampling effort.

A baseline mapping of *Pinna nobilis* individuals in OA and CV was performed using area-specific methodologies to optimize performance under local conditions. In both areas, each plot was initially delimited with ground lines. Vertex coordinates were recorded with a Hemisphere S631 GNSS receiver operating in Real-Time Kinematic (RTK), enabling the calculation of the actual surface area and the repositioning of ground lines in subsequent surveys. High-resolution waterproof maps (with an estimated positioning error of about 20 cm) were produced for each plot to relocate the individuals.

In the OA plots, individuals were mapped from high-resolution orthophoto mosaics based on underwater Structure-from-Motion (SfM) photogrammetry.[65] The photogrammetric survey for plot A was conducted in October 2020 and for plots B and C between March and April 2023. The plot areas resulted 115.4 m^2, 125.5 m^2, and 133.4 m^2, respectively. Initial status (either live or dead) and biometrics for all individuals were assessed on 16 and 30 March 2023. Main shell biometrics[40] were acquired with a custom-designed caliper (resolution of 0.5 cm), including the width at the maximum dorso-ventral shell amplitude (W_{max}) and the unburied shell length (UL). Shell degradation was also assessed and categorized as follows: intact and with negligible fouling on the shell margin (recently deceased specimens, on a timescale spanning from days to two weeks); chipped (with all biometrics still measurable); heavily damaged (UL not reliable); and broken at the base (W_{max} not measurable). The status of the live individuals was assessed over two summers, with surveys at intervals of 2-3 months on the following dates: 30-31/05/2023, 26-

28/07/2023, 25/09/2023, 27/11/2023, 20/02/2024, 17/05/2024, 18 and 30/07/2024, and 7/10/2024.

In the CV area, which was added in 2024 to establish a comparative framework with the existing OA dataset, the baseline surveys were conducted on 14, 17, and 23 May 2024, when the three plots were delineated and all the individuals mapped. In this case, individuals were georeferenced directly with a Hemisphere S631 GNSS receiver operating in RTK. The surface areas of the three plots A, B and C resulted respectively 116.4 m^2, 107.3 m^2, and 100.5 m^2. Concurrently, the status and biometrics of the individuals were recorded following the approach previously described. The status of the live individuals was assessed again on 31 July – 1 August and on 11 and 14 October. To extend the comparison to OA data, the February 2024 status for the CV population was approximated by classifying all specimens with intact shells in May as live at that time.

All the field activities were performed by snorkel divers. The applied protocols do not involve the sampling/collection of specimens, nor other invasive procedures.

The size structure of the populations was analyzed based on Total shell length (TL), derived from W_{max} using the model proposed by García-March[66], $TL = 1.29 \times W_{max}^{1.24}$. The model was selected for its relevance to lagoon populations. The analysis excluded shells broken at the base due to unreliable TL estimation. TL histograms (2-cm breaks) as well as kernel density plots were produced for the pooled live and dead individuals, and for live individuals only, contrasting study areas and moments in time (March 2023, February 2024 and October 2024).

Size-specific relative mortality was assessed as the proportion of individuals that died over an eight-month period encompassing the summer mortality peaks (using the 2023 and 2024 datasets for OA, and the 2024 dataset for CV), based on 10-cm size classes. To investigate the relationship between size and mortality, regression analyses were performed with the center of each class as the independent variable, using both Linear Models (LM) and Generalized Linear Models (GLM) with a quasibinomial family to capture potential non-linear relationships. Model performances were compared using the Root Mean Square Error (RMSE).

The statistical analyses were performed with the R environment.[67]

6.3 Environmental characterization

To characterize the environmental conditions of the two study areas, temperature, salinity, and dissolved oxygen (DO) were monitored throughout the survey period. Continuous data (5-min interval) were acquired using conductivity and DO data loggers, about 10-20 cm above the seabed. Conductivity loggers (HOBO U24) were deployed in OA on 31 May 2023 and in CV on 20 June 2024, while DO logger (HOBO U26) were deployed in OA and CV on 17 and 20 June 2024, respectively. Sensors were cleaned and calibrated periodically every about one month. Outliers (values < Q1−3×IQR or > Q3+3×IQR, where Q1 is 1st quartile, Q3 is 3rd quartile and IQR is interquartile range) and unreliable data were removed and, when possible, replaced through linear interpolation.

5.4 Hemocyte and tissue sampling in Ottagono Alberoni and Coffa Val Grande

Due to its status as an endangered and protected species, sampling of *P. nobilis* was carried out under the permission of regional and national Authorities for animal welfare (Prot. MATTM 0016478 05/03/2020 Ref.: Prot. 28494, renewed in 2023, Prot. MASE 0208559 del 19/12/2023). In May 2023, hemolymph was collected from 8 individuals and the 100% diagnosed with *Pinna nobilis* Picornavirus.[26] Following this discovery, 8 Mantle biopsies (0.5 cm2) were taken using Schumacher biopsy forceps and preserved in RNAlater (Thermo Fisher Scientific) in February 2024. After, a total of 28 animals were sampled in Ottagono Aberoni and Coffa Val Grande areas for two consecutive seasons in May and July 2024, sampling the same animals over all the seasons when possible **(Tab. 1-2).**

Table 1. Samples of mantle collected in Coffa Val Grande (CV) in February 2024.

AREA OF SAMPLING	SAMPLE CODE MANTLE 2024
CV	Pn1_CVF24
CV	Pn2_CVF24
CV	Pn3_CVF24
CV	Pn4_CVF24
CV	Pn5_CVF24
CV	Pn6_CVF24
CV	Pn7_CVF24
CV	Pn8_CVF24

Table 2. Sampling areas and animals code of the samples collected in Ottagono Alberoni (OA) and Coffa Val Grande (CV) in May and July 2024. **In bold:** the animals sampled in both the seasons.

Sampling Area	Sample code May	Sample code July	Sample code July (mantle)	Animal max lenght (cm)
OA	Pn1_OAM24			53 x 17
OA	**Pn2_OAM24**	**Pn2Old_OAJ24**		51 x17
OA	Pn3_OAM24			48 x16
OA	Pn4_OAM24			61x19
OA	**Pn5_OAM24**	**Pn5Old_OAJ24**	**Pn5Old_OAJ24M**	64X22
OA	Pn6_OAM24			56 X16
OA	Pn7_OAM24			48 x 18
OA	Pn8_OAM24			65 x 22
OA		Pn1New_OAJ24		57 x 18
OA		Pn2New_OAJ24		54 x 13
CV	**Pn1_CVM24**	**Pn1Old_CVJ24**		38 x 30
CV	Pn2_CVM24			44 x 25
CV	**Pn3_CVM24**	**Pn3Old_VJ24**		52 x 19
CV	Pn4_CVM24			38 x 14
CV	Pn5_CVM24			35 x 13

CV	Pn1New_CVJ24	51 x 19
CV	Pn2New_CVJ24	45 x 20
CV	Pn3New_CVJ24	54 x 15

Animals were measured for the maximal valve length. Hemolymph was collected via a 21-gauge needle from the anterior adductor muscle as a non-destructive sampling. According to Carella et al.[26], the specimens were gently detached from the substrate and brought to surface level to allow hemolymph to be withdrawn from the anterior adductor muscle that lies at the tip of the valves. Presence of disease symptoms were considered during sampling. The procedure was performed carefully to minimize animal stress. Adductor muscle was gently penetrated with a 21-gauge needle directed along a line parallel to the anterior edge of the shell valves, as reported by Carella et al.[26] After the procedure, the animals were immediately relocated to the seabed, and the health state was monitored over the following days. A volume of ~2 ml of hemolymph was collected for each animal. A 1 ml hemolymph aliquot was placed in a 1 ml RNA Later (Sigma-Aldrich, Italy)-labeled tube placed on ice for molecular analyses, and the other half was preserved for ultrastructural analyses. A small hemolymph aliquot (20 µl) was placed on a hemocytometer (Burker chamber) to determine the total cell number ($\times 10^5$/ml) and define the total hemocyte count (THC). Other 50ul were put on a slide for cytology.

5.4.1 Cytology

Glass slides with fixed hemocytes were stained with May-Grunwald-Giemsa (MGG), for basic proteins detection (Bio-Optica, Italy) and observed at the microscope. Identification of different morphotypes of hemocytes and nucleus staining and evaluation of cytoplasm color and its intensity.

5.4.2 Semithin sections and Transmission Electron Microscopy (TEM)

For all the animals collected in 2024, part of the hemolymph was also fixed in glutaraldehyde 2,5% in PBS for 3 h. Cells were postfixed in 1% osmium tetroxide for 60 min and 0.25% uranyl

649 acetate overnight. They were dehydrated through a graded ethanol series and embedded in EPON
650 resin overnight at 37 °C, 1 day at 45 °C and 1 day at 60 °C. Semi-thin sections (0.75 µm) were
651 prepared using a HM-360 rotary microtome (MICROM International GmbH, Germany) and
652 stained with methylene blue, then analyzed using a camera Axiocam 208 colour mounted on a
653 Axioscope 5 (Carl Zeiss, Germany) microscope connected to a computer. Estimation of number of
654 death cells (absence of nucleus or fragmented nucleus) was evaluated over 100 cells and
655 expressed as percentage. Ultrathin sections (80 nm) were cut parallel to the substrate and placed
656 onto a 200-mesh copper grid. Bright-field TEM images were obtained on the dried sample by
657 using a FEI TECNAI G2 200 kV s-twin microscope operating at 120 kV (Thermo Fisher Scientific,
658 Waltham, USA). Digital images were acquired with an Olympus VELETA camera.
659
660 **5.5. Immunoblotting analysis and Caspase-3 activation assay**
661
662 Total proteins from hemocytes from 2024, and tissues such as gonad, mantle and gill and
663 hemocytes from 3 moribund animals sampled in Venice in 2021 were obtained with RIPA Buffer
664 containing 1x protease inhibitor, 1x PMSF and 1x Na3VO4. Lysates were clarified by centrifugation
665 at 12000g for 30' at 4°C. 30µg of each sample was separated by SDS-PAGE and subjected to
666 western blot. The nitrocellulose membranes were immunoblotted with antibodies against *active*
667 *Caspase-3* (clone C92-605, BD, bioscience) and GADPH (E-AB-40337, ElabScience) at the dilution
668 of 1:1000 in 3% BSA in T-TBS (0,1% tween in TBS) overnight. After incubation with peroxidase-
669 conjugated anti-mouse and/or anti-rabbit antibodies (1:5000; Amersham-Biosciences), proteins
670 were revealed by an ECL kit (Millipore). Band intensity was quantified by Image Lab Software
671 ChemiDoc (BioRad).
672 Apoptotic cells were detected using a FITC Active Caspase 3 Apoptosis kit (550480 BD Bioscience)
673 which selectively recognize the active form of caspase-3 in cells following the manufacture's
674 recommendations. Briefly, 1x10^6 cells, previously stored at 4°C in 2,5% glutaraldehyde, were
675 washed twice with cold 1X PBS, then incubated in BD Cytofix/CytopermTM solution at a
676 concentration of 1x10^6 cells/0.5 ml for 20 min on ice. After two Perm/WashTM buffer (1X)
677 washes, cells were incubated with 10µl of anti-Caspase 3 antibody and 10µg/ml Propidium Iodide

(PI) for 30 min at room temperature. Fluorescence was determined by using Accuri C6 Flow Cytometer (Becton Dickinson, Franklin Lakes, NJ, USA). At least 15000 total events were acquired, of which 5000 events were PI positive and analyzed. All data were analyzed with Floreada.io online software WASM Version: SIMD (accessed May, 2025).

5.6 RNA and DNA isolation, real time PCR, end point PCR and sequencing

Simultaneous isolation of DNA and RNA from immune cells was performed to accomplish both evaluation of DNA and RNA pathogens. Total RNA and DNA were extracted from the hemocytes using the PureLink RNA Mini Kit (Thermo Fisher Scientific, Waltham, Massachusetts, USA) eluted in 50µl. DNase treatment was performed on all the individuals in a volume of 20ul. RNA quantification was then performed using the Nanodrop 2000 spectrophotometer (Thermo Fisher Scientific). RNA (~500 ng) was reverse transcribed using Maxima First Strand cDNA Synthesis (Thermo Scientific). Specific primers for *PnPv* were used and a quantitative real-time PCR reaction was performed as reported by Carella et al.[26] Amplification reactions were performed in a total volume of 10 µl using 5 µl of PowerUp SYBR Green Master Mix (Applied Biosystems), 0.2 µM of each specific primer, and adjusted to 10 µl with distilled water. The reactions were conducted in technical duplicates using bivalve 18S rRNA as a reporter gene.[68] The amplification conditions used were as follows: 1 cycle for 2 min at 50◦C; 1 cycle for 2 min at 95◦C; 40 cycles of amplification at 95◦C for 15 s; 60◦C for 18 s; and 72◦C for 1 min. The reactions were conducted in the QuantStudio 3 Real-Time PCR System (Thermo Scientific). Two positive controls were used, and two negative controls were run without cDNA. PCR amplifications were conducted on cDNA using the primer pair ChaetoF1 5’-AGGGATGTTTGTGGGAGCAC-3’ and ChaetoR1 5’-ACCGCCGAGGGTATTCTACT-3’.

End point PCR were conducted as follows: 1 cycle for 3 min at 95◦C; 35 cycles of amplification at 95◦C for 30s, 58◦C for 30 s and 72◦C for 30 s with a final extension of 72°C for 7 minutes. The amplified fragments (193 bp) were separated using electrophoresis on 2% agarose gel in 1X TAE buffer. Sanger sequencing was performed of the obtained products (Eurofin Genomics, Germany).

After BLAST checking, the sequences were deposited in GenBank (accession numbers: PZ407978-PZ407985).

DNA quality and quantity were checked with a Nanodrop ND-1000 spectrophotometer (Nanodrop spectrophotometer, Monza, Italy). The primer pairs HPNF3/HPNR3 were used to detect the presence of *H. pinnae* with the thermal cycle and conditions as reported by Catanese et al.[69] For Mycobacterium, primers derived from the 16S rRNA sequence of mycobacteria, mycgen-f / mycgen-r, as described by Böddinghaus et al.[70], were used. Positive controls were used for both the PCR reactions. The amplification products were separated using electrophoresis on 2% agarose gel in 1X TAE buffer. Sanger sequencing was performed of the obtained products (Eurofin Genomics, Germany).

Statistical analyses were performed with GraphPad Prism version 8.0 (GraphPad Software). The correlations between biological and environmental variables were evaluated by a Spearman rank correlation test. Wilcoxon's signed-rank test was used for matched pairs. Mann-Whitney U tests were used for comparison between 2 groups of data. P values less than *0.05* were considered to indicate statistical significance.

5.7 *PnPV* phylogeny

A nucleotide alignment was performed using the 193 bp fragments of PnPv obtained in this study, the corresponding fragments amplified from two samples from Sicily (Accession: PZ407986-87), and representative sequences available in GenBank. The alignment was produced with ClustalW, and the Neighbor-Joining (NJ) tree was inferred using the Jukes–Cantor model implemented in MEGA X (Kumar et al., 2018), with 1000 bootstrap replicates.

Funding

The author(s) declared financial support was received for the research, authorship, and/or publication of this article. The research was supported by the EU LIFE Programme Project Protection and restoration of *Pinna nobilis* populations as a response to the catastrophic

pandemic started in 2016 (LIFE PINNARCA) (grant number LIFE20 NAT/ES/001265) and LIFE PINNACARE Project for Manuscript finalization.

Acknowledgments

The authors thank Dr. Sergio Sorbo of the CeSMA, Section of Microscopy LaMMEC, University of Naples Federico II, and Dr. Antonella Giarra, Chemistry Department of the University of Naples Federico II, for technical support in electron microscopy. The authors also thank Alessandro Bergamasco, CNR-ISMAR Venice, for his valuable assistance with environmental data acquisition and processing and Roberto Vianello and Loris Dametto (CNR-ISMAR) for technical assistance during fieldwork sampling in Venice.

Author contribution statement:

FC: Conceptualization; resources; visualization; supervision; manuscript organization; performing analysis; data curation; writing, Review & Editing; project Administration; funding Acquisition; **AF:** performing analysis; data curation, Review & Editing ; **GR:** performing analysis, data curation, Review & Editing; SA: performing analysis; data curation; writing; **JGM:** writing, Review & Editing; **JTM:** writing, Review & Editing; **PP:** Resources, writing, Review & Editing; **GM:** performing analysis; **AS:** performing analysis; **MS:** visualization; performing analysis; data curation; Review & Editing

The authors declare that they have no known competing financial interests or personal relationships that could have appeared to influence the work reported in this paper.

Data availability

The datasets generated and/or analyzed during the current study are available in the GenBank repository, accession numbers: PZ407978- PZ407987.

763

764

765 **References**

766

767 1. Vijayakrishnan, S., Jiu, Y. & Harris, J. R. *Virus Infected Cells*. (Springer, 2023).

768 2. Miller, S. & Krijnse-Locker, J. Modification of intracellular membrane structures for virus
769 replication. *Nat. Rev. Microbiol.* **6**, 363–374 (2008).

770 3. Graessmann, A., Graessmann, M., Tjian, R. & Topp, W. C. Simian virus 40 small-t protein is
771 required for loss of actin cable networks in rat cells. *J. Virol.* **33**, 1182–1191 (1980).

772 4. Taylor, M., Koyuncu, O. & Enquist, L. Subversion of the actin cytoskeleton during viral infection.
773 *Nat. Rev. Microbiol.* **9**, 427–439 (2011).

774 5. Vitale, I., et al. Apoptotic cell death in disease—Current understanding of the NCCD 2023. *Cell*
775 *Death Differ.* **30**, 1097–1154 (2023).

776 6. Mace, P. D. & Riedl, S. J. Molecular cell death platforms and assemblies. *Curr. Opin. Cell Biol.*
777 **22**, 828–836 (2010).

778 7. Young, M. M., Kester, M. & Wang, H.-G. Sphingolipids in antiviral defense and viral
779 pathogenesis. *J. Virol.* **94**, e01265-19 (2020).

780 8. Reshi, M. L., Su, Y.-C. & Hong, J.-R. RNA viruses: ROS-mediated cell death. *Int. J. Cell Biol.* **2014**,
781 467452 (2014).

782 9. Nainu, F., Shiratsuchi, A. & Nakanishi, Y. Induction of apoptosis and subsequent phagocytosis
783 of virus-infected cells as an antiviral mechanism. *Front. Immunol.* **8**, 1220 (2017).

784 10. O'Brien, V. Viruses and apoptosis. *J. Gen. Virol.* **79**, 1833–1845 (1998).

785 11. Vogeler, S., Carboni, S., Li, X. & Joyce, A. Phylogenetic analysis of the caspase family in bivalves:
786 implications for programmed cell death, immune response and development. *BMC Genomics*
787 **22**, 80 (2021).

788 12. Li, C., et al. Cloning and characterization of a novel caspase-8-like gene in *Crassostrea gigas*.
789 *Fish Shellfish Immunol.* **46**, 486–492 (2015).

790 13. Romero, A., Estevez-Calvar, N., Dios, S., Figueras, A. & Novoa, B. New insights into the
791 apoptotic process in mollusks: characterization of caspase genes in *Mytilus galloprovincialis*.
792 *PLoS One* **6**, e17003 (2011).

14. Zhang, L., Li, L. & Zhang, G. Gene discovery, comparative analysis and expression profile reveal the complexity of the *Crassostrea gigas* apoptosis system. *Dev. Comp. Immunol.* **35**, 603–610 (2011).

15. Lu, Y., Li, J., Zhang, Y., Zhang, Y. & Xiang, Z. Molecular characterization and functional analysis of a caspase-1 homologue from the oyster *Crassostrea hongkongensis*. *Fish Shellfish Immunol.* **60**, 271–279 (2017).

16. Yang, B., et al. Molecular cloning of two molluscan caspases and gene functional analysis during *Crassostrea angulata* (Fujian oyster) larval metamorphosis. *Mol. Biol. Rep.* **42**, 963–975 (2014).

17. Xu, J., et al. Caspase-3 serves as an intracellular immune receptor specific for lipopolysaccharide in oyster *Crassostrea gigas*. *Dev. Comp. Immunol.* **61**, 1–12 (2016).

18. Romero, A., Novoa, B. & Figueras, A. The complexity of apoptotic cell death in mollusks: An update. *Fish Shellfish Immunol.* **46**, 79–87 (2015).

19. Kiss, T. Apoptosis and its functional significance in molluscs. *Apoptosis* **15**, 313–321 (2010).

20. Thornberry, N. A. The caspase family of cysteine proteases. *Br. Med. Bull.* **53**, 478–490 (1997).

21. Sokolova, I. M., Evans, S. & Hughes, F. M. Cadmium-induced apoptosis in oyster hemocytes involves disturbance of cellular energy balance but no mitochondrial permeability transition. *J. Exp. Biol.* **207**, 3369–3380 (2004).

22. Lacoste, A., Cueff, A. & Poulet, S. A. P35-sensitive caspases, MAP kinases and Rho modulate b-adrenergic induction of apoptosis in mollusc immune cells. *J. Cell Sci.* **115**, 761–768 (2002).

23. Katsanevakis, S., et al. in *Imperiled: the Encyclopedia of Conservation* (eds. Dellasala, D. A. & Goldstein, M. I.) (Elsevier, 2022).

24. Carella, F., et al. A widespread picornavirus affects the hemocytes of the noble pen shell (*Pinna nobilis*), leading to its immunosuppression. *Front. Vet. Sci.* **10**, 1273521 (2023).

25. Prado, P., et al. *Pinna nobilis* in suboptimal environments are more tolerant to disease but more vulnerable to severe weather phenomena. *Mar. Environ. Res.* **163**, 105220 (2021).

26. Carella, F., et al. Multi-pathogen infections and multifactorial pathogenesis involved in noble pen shell (*Pinna nobilis*) mass mortality events: background and current pathologic approaches. *Vet. Pathol.* **61**, 3009858231186737 (2023).

27. Carella, F., et al. Measuring immunocompetence in the natural population and captive individuals of noble pen shell *Pinna nobilis* affected by *Pinna nobilis* Picornavirus (PnPV). *Fish Shellfish Immunol.* **151**, 109664 (2024).

28. Iaria, C., et al. Cytopathology and phylogeny of *Pinna nobilis* Picornavirus (PnPV) infecting haemocytes of the noble pen shell population from Lake Faro (Southern Italy). *J. Invertebr. Pathol.* **208**, 108381 (2025).

29. Sigovini, M., et al. The last stronghold in the Adriatic: Distribution and status of *Pinna nobilis* in the Venice lagoon. in *Proc. 43rd CIESM Congress* 11 (2024).

30. Olivi, G. *Zoologia Adriatica ossia catalogo ragionato degli Animali del Golfo e delle Lagune di Venezia*. (Bassano, 1792).

31. Coen, G. *Nota sui Molluschi della Laguna Veneta*. (Società Italiana per il progresso delle scienze, 1938).

32. Cesari, P. *Itinerari culturali nel veneziano, la Laguna. Tomo 1°*. (Corbo e Fiore Editori, 1992).

33. Cesari, P. *I Molluschi della Laguna di Venezia*. (Arsenale Editrice, 1994).

34. Chiereghin, S. *Descrizione de' Pesci, de' Crostacei e de' Testacei che abitano le Lagune ed il Golfo Veneto*. (Canova ed., 2001).

35. Russo, P. Lagoon malacofauna: results of malacological research in the Venice Lagoon. *Boll. Malacol.* **53**, 49–62 (2017).

36. Chang, K., et al. Filopodia and viruses: An analysis of membrane processes in entry mechanisms. *Front. Microbiol.* **7**, 300 (2016).

37. Šiletić, T. & Peharda, M. Population study of the fan mussel *Pinna nobilis* L. in Malo and Veliko Jezero of the Mljet National Park (Adriatic Sea). *Sci. Mar.* **67**, 91–98 (2003).

38. Katsanevakis, S. Population ecology of the endangered fan mussel *Pinna nobilis* in a marine lake. *Endanger. Species Res.* **3**, 297–304 (2007).

39. Tempesta, M., et al. Distribution, density and size class structure of a population of the fan mussel *Pinna nobilis* (Linnaeus, 1758) in the Marine Protected Area "Isole Egadi" (Sicily, Italy). *Acta Adriat.* **54**, 271–280 (2013).

40. García-March, J. R. & Vicente, N. in *Monitoring of Mediterranean marine protected areas* (MedPAN Project, 2007).

41. Basso, L., Hendriks, J. R. & Duarte, C. M. The Pen Shell, *Pinna nobilis*: A review of population status and recommended research priorities in the Mediterranean Sea. *Adv. Mar. Biol.* **71**, 109–160 (2015).

42. Cabanellas-Reboredo, M., et al. Tracking a mass mortality outbreak of pen shell *Pinna nobilis* populations: A collaborative effort of scientists and citizens. *Sci. Rep.* **9**, 13355 (2019).

43. Šarić, T., Župan, I., Čižmek, H., Grossel, H. & Jaklin, A. Mass mortality of the fan mussel *Pinna nobilis* in the Adriatic Sea: Assessment of population decline and health status. *Front. Mar. Sci.* **11**, 1345678 (2024).

44. Lattos, A., et al. Investigation of the highly endangered *Pinna nobilis'* mass mortalities: Seasonal and temperature patterns of health status, antioxidant and heat stress responses. *Mar. Environ. Res.* **188**, 105977 (2023).

45. García-March, J. R., et al. Signal of a mass mortality event in *Pinna nobilis* populations based on temperature thresholds. *Front. Mar. Sci.* **7**, 582878 (2020).

46. Longo, S., Gristina, M. G., Garofalo, G. & Maltagliati, F. Effects of hypoxia on the respiration rate, food consumption and assimilation efficiency in Mediterranean bivalves. *Mar. Ecol. Prog. Ser.* **354**, 121–130 (2008).

47. Song, J., et al. Impact of anthropogenic global hypoxia on the physiological response of bivalves. *Sci. Total Environ.* **926**, 172056 (2024).

48. Basso, L., Hendriks, I. E. & Duarte, C. M. Juvenile *Pinna nobilis* tolerance to moderate hypoxia. *Estuaries and Coasts* **38**, 1234–1245 (2015).

49. Peyran, C., et al. High genetic diversity and potential for local adaptation in surviving populations of the endangered noble pen shell *Pinna nobilis*. *Sci. Rep.* **12**, 14234 (2022).

50. Martínez-Martínez, P., et al. Looking for the surviving optimal areas for the threatened species *Pinna nobilis* in a highly anthropized coastal lagoon (Mar Menor, SE Spain). *Ocean Coastal Manage.* **255**, 107265 (2024).

51. Allam, B. & Raftos, D. Immune responses to infectious diseases in bivalves. *J. Invertebr. Pathol.* **131**, 121–136 (2015).

52. Matozzo, V. & Bailo, L. A first insight into haemocytes of the smooth venus clam *Callista chione*. *Fish Shellfish Immunol.* **42**, 494–502 (2015).

53. Nakayama, K., Nomoto, A. M., Nishijima, M. & Maruyama, T. Morphological and functional characterization of hemocytes in the giant clam *Tridacna crocea*. *J. Invertebr. Pathol.* **69**, 105–111 (1997).

54. Matozzo, V., Pagano, M., Spinelli, A., Caicci, F. & Faggio, C. *Pinna nobilis*: a big bivalve with big haemocytes? *Fish Shellfish Immunol.* **55**, 529–534 (2016).

55. Bustamante, J., et al. From infectious diseases to primary immunodeficiencies. *Immunol. Allergy Clin. North Am.* **28**, 235–258 (2008).

887 56. Hongo, Y. & Tomaru, Y. Transcriptomic insights into host transcriptional manipulation by
888 ssDNA and ssRNA viruses in the marine planktonic diatom *Chaetoceros tenuissimus*. *Virus Res.*
889 **351**, 199605 (2025).

890 57. Yin-Murphy, M. & Almond, J. W. in *Medical Microbiology* (ed. Baron, S.) (University of Texas
891 Medical Branch, 1996).

892 58. Tuthill, T. J., Groppelli, E., Hogle, J. M. & Rowlands, D. J. Picornavirus entry. *Curr. Top. Microbiol.*
893 *Immunol.* **343**, 43–89 (2010).

894 59. Oliveira, A. C., et al. Low temperature and pressure stability of picornaviruses: implications for
895 virus uncoating. *Biophys. J.* **76**, 1270–1279 (1999).

896 60. Asadi, M., Taghizadeh, S., Kaviani, E., et al. Caspase-3: Structure, function, and
897 biotechnological aspects. *Biotechnol. Appl. Biochem.* **69**, 1633–1645 (2022).

898 61. Lehmann, M. J., et al. Actin- and myosin-driven movement of viruses along filopodia precedes
899 their entry into cells. *J. Cell Biol.* **170**, 317–325 (2005).

900 62. Oh, M. J., et al. Role of heparan sulfate in herpes simplex virus 1 entry, surfing, and filopodia
901 formation. *J. Virol.* **84**, 9022–9032 (2010).

902 63. Agelidis, A. M. & Shukla, D. Cell entry mechanisms of HSV: what we have learned in recent
903 years. *Future Virol.* **10**, 1145–1154 (2015).

904 64. Tagliapietra, D., Cornello, M. & Pessa, G. Indirect estimation of benthic secondary production
905 in the Lagoon of Venice (Italy). *Hydrobiologia* **588**, 205–212 (2007).

906 65. Sabino, A., Bergamasco, A., Scarpa, G. M. & Sigovini, M. An innovative photogrammetric
907 approach for the monitoring of the endangered fan mussel *Pinna nobilis*: a case study from
908 the Venice Lagoon. *Reg. Stud. Mar. Sci.* (submitted).

909 66. García-March, J. R. *Aportaciones al Conocimiento de La Biologìa de Pinna nobilis Linneo, 1758*
910 *(Mollusca Bivalvia) En El Litoral Mediterràneo Ibérico*. (Universitat de Valencia, 2005).

911 67. R Core Team. *R: A Language and Environment for Statistical Computing*. (R Foundation for
912 Statistical Computing, 2025).

913 68. Aceto, S., Formisano, G., Carella, F., De Vico, G. & Gaudio, L. The metallothionein genes of
914 *Mytilus galloprovincialis*: genomic organization, tissue expression and evolution. *Mar.*
915 *Genomics* **4**, 61–68 (2011).

916 69. Catanese, G., et al. *Haplosporidium pinnae* sp. nov., a haplosporidan parasite associated with
917 mass mortalities of the fan mussel, *Pinna nobilis*, in the Western Mediterranean Sea. *J.*
918 *Invertebr. Pathol.* **157**, 9–24 (2018).

70. Böddinghaus, B., et al. Detection and identification of mycobacteria by amplification of rRNA. *J. Clin. Microbiol.* **28**, 1751–1759 (1990).

Figures and Tables legends:



Figure 1. Map of the Venice lagoon with circles indicating the position of the two study areas Ottagono Alberoni (OA) and Coffa Val Grande (CV).

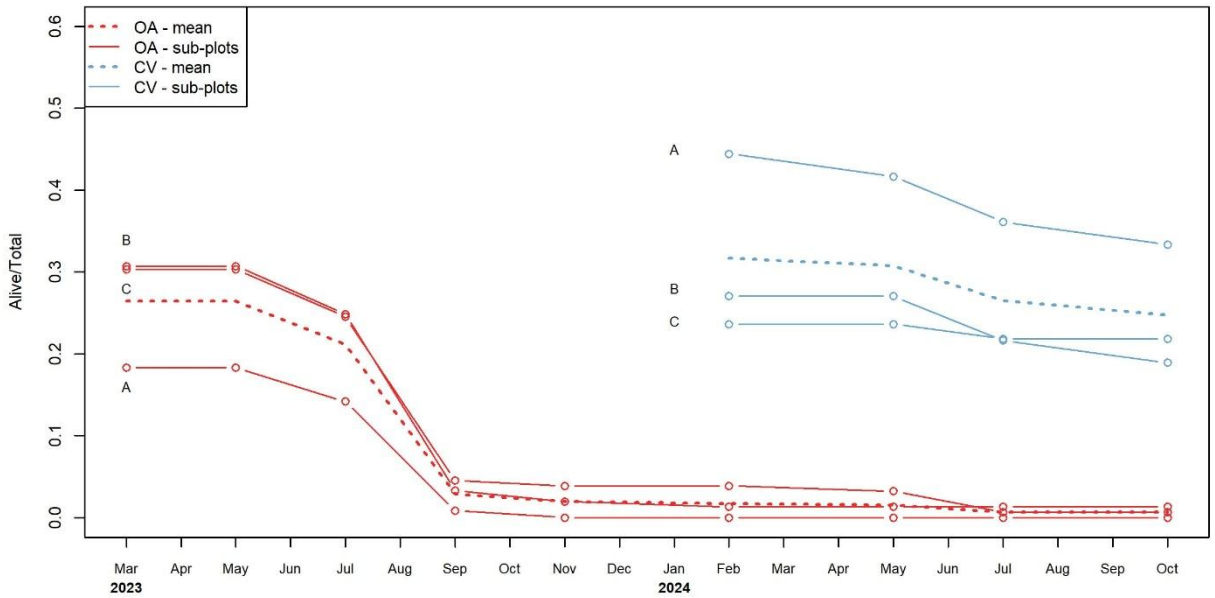
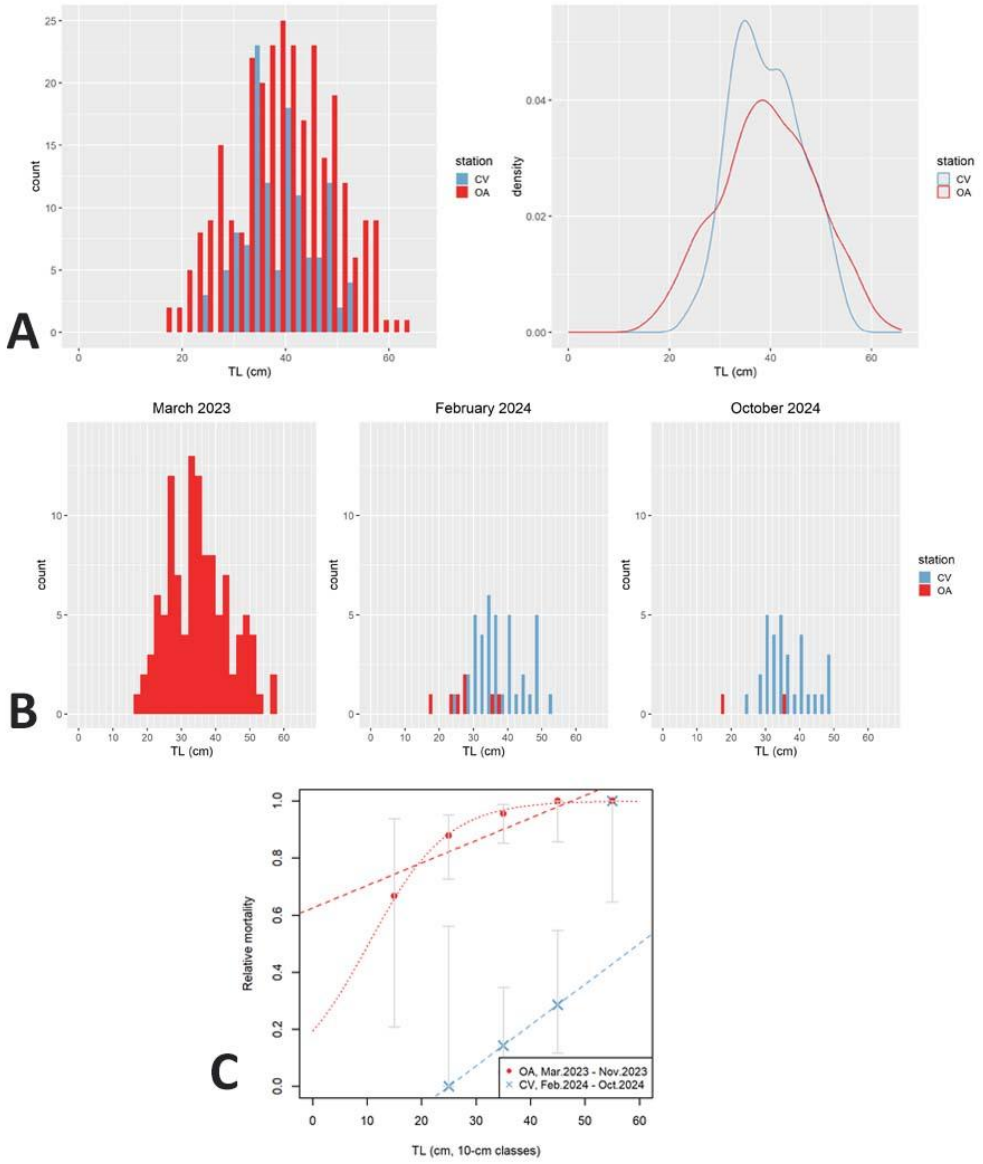


Figure 2. Temporal trends in survival rates (as live-to-total ratio) at the Ottagono Alberoni (OA) and Coffa Val Grande (CV) areas in 2023-2024.

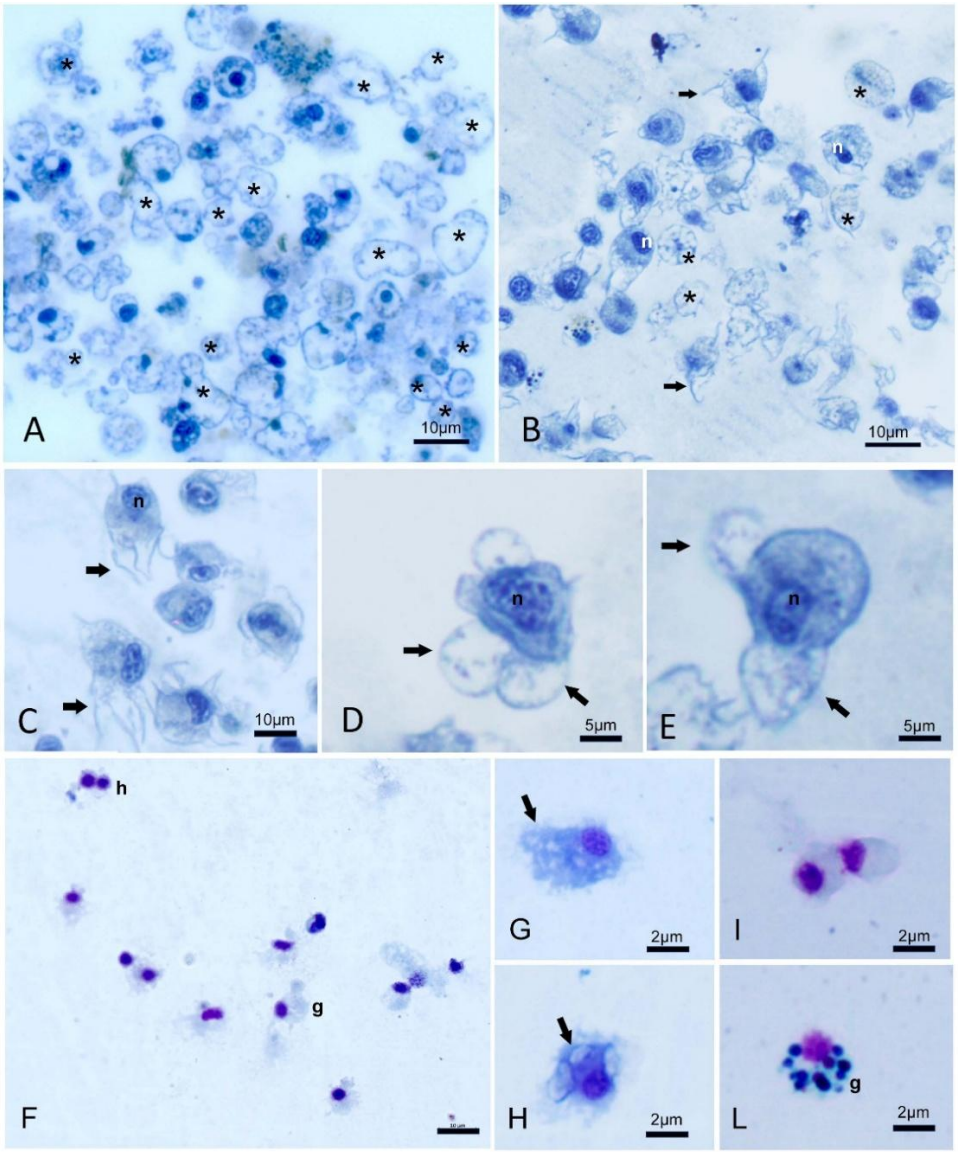
928



929

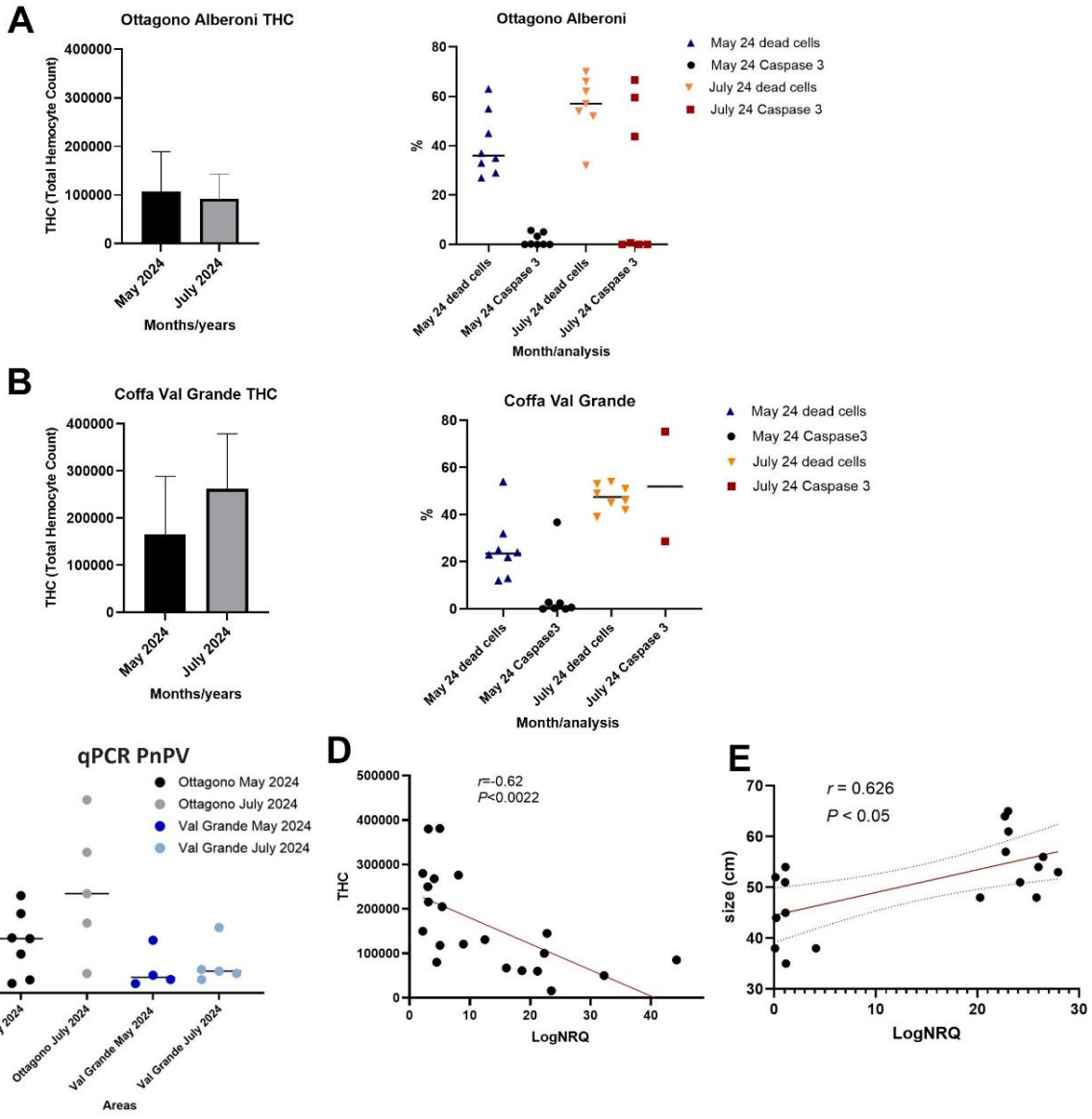
930 **Figure 3. A.** Histogram and kernel density plot of estimated total length (TL) for all the individuals (live and
931 dead) of Ottagono Alberoni (OA) and Coffa Valgrande (CV). **B.** Histogram of estimated total length (TL) for
932 live individuals of Ottagono Alberoni (OA) and Coffa Valgrande (CV); **C.** Relative mortality over eight-
933 months periods for 10-cm size classes across the two study areas and two years. Points indicate mortality
934 fractions for dataset D1 (black circles) and dataset D3 (red triangles) with 95% Wilson score confidence
935 intervals. Linear regressions (dashed lines) and GLM (logit link) fits for the 2023 OA and 2024 CV datasets
936 are shown.

937



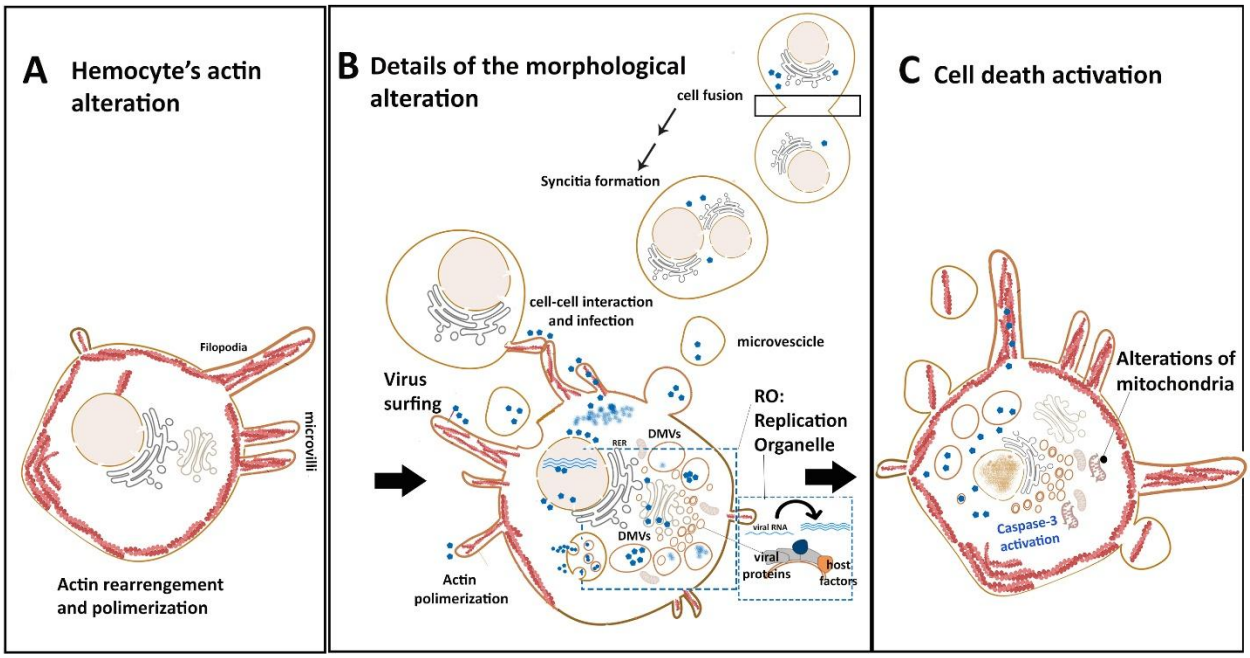
938
939

940 **Figure 4.** Light micrograph of *Pinna nobilis* hemocyte semi-thin sections stained with methylene blue (**A-**
941 **E**) and cytology stained with MGG (**F-L**); in images **A** and **B** of cell status representatives of May and July
942 2024 in both OA and CV with dead cells and apoptotic bodies (*) with no nucleus or displaying projections
943 (arrows in B); **C**, cells display filopodia and blebs (**D-E**); **F.** MGG stain shows hemocytes types, granulocytes
944 (g) and hyalinocytes (h) and details of cells displaying large vacuoles in **G-H** and with visible darken dots
945 (g) in **L**.



946

947 **Figure 5. THC and activation of caspase-3 in *Pinna nobilis* immune cells during *PnPv* infection. A-B**
948 Representative graphs show THC and dead cells in OA and CV in May and July 2024 and active caspase-3
949 expression in hemocytes cells. **C.** Real-time PCR of *PnPv* performed on the immune cells in the two areas
950 and moths. Each dot represents a single individual, and associations were evaluated using Pearson's
951 correlation test (**D-E)**. P values are presented. *P < 0.05, **P < 0.01, ***P < 0.001. pos, positive.



952
953

954 **Figure 6. Schematic of the mechanism of *PnPv* infection in *Pinna nobilis* hemocytes in Venice lagoon and**
955 **related cytopathic effects.** **A.** Virus Infecting cells induces cell structural alterations with filopodia or
956 microvilli formation due to actin polymerization; filopodia are actin-rich structures that contain
957 polymerized actin packages induced by the virus to support his life cycle.[36] **B.** Actin is remodeled along the
958 viral life cycle and used for viral particle passage and movement (surfing) to infect other cells inducing a
959 cell-cell interaction. Virus can also induce syncytia formation (cell fusion) as reported also by Carella et
960 al.[27] At the level of the cytoplasm, the Replication Organelle (RO) (**large blue dotted square**) is the most
961 evident feature and seems to originate by a remodeled ER and nuclear membrane interacting with a Golgi
962 complex compartment creating DMVs of different dimensions where viral replication takes place. The RO
963 is reported to be constituted by both viral and host factors (**small blue dotted square**). Infectious exosomes
964 and budding extracellular vesicles were also visible as previously reported by Carella et al.[26] *PnPV* can also
965 actively interact with the host nucleus to facilitate infection using nuclear pores. **C.** Damage to
966 mitochondria and virus entrance in the nucleus can activate apoptosis, displayed as visible morphological
967 alteration with cell shrinkage nuclear condensation (pyknosis) and membrane blebbing with formation of
968 apoptotic bodies. This phase is activated by the executor final active caspase-3 after the initiator caspases.
969
970
971

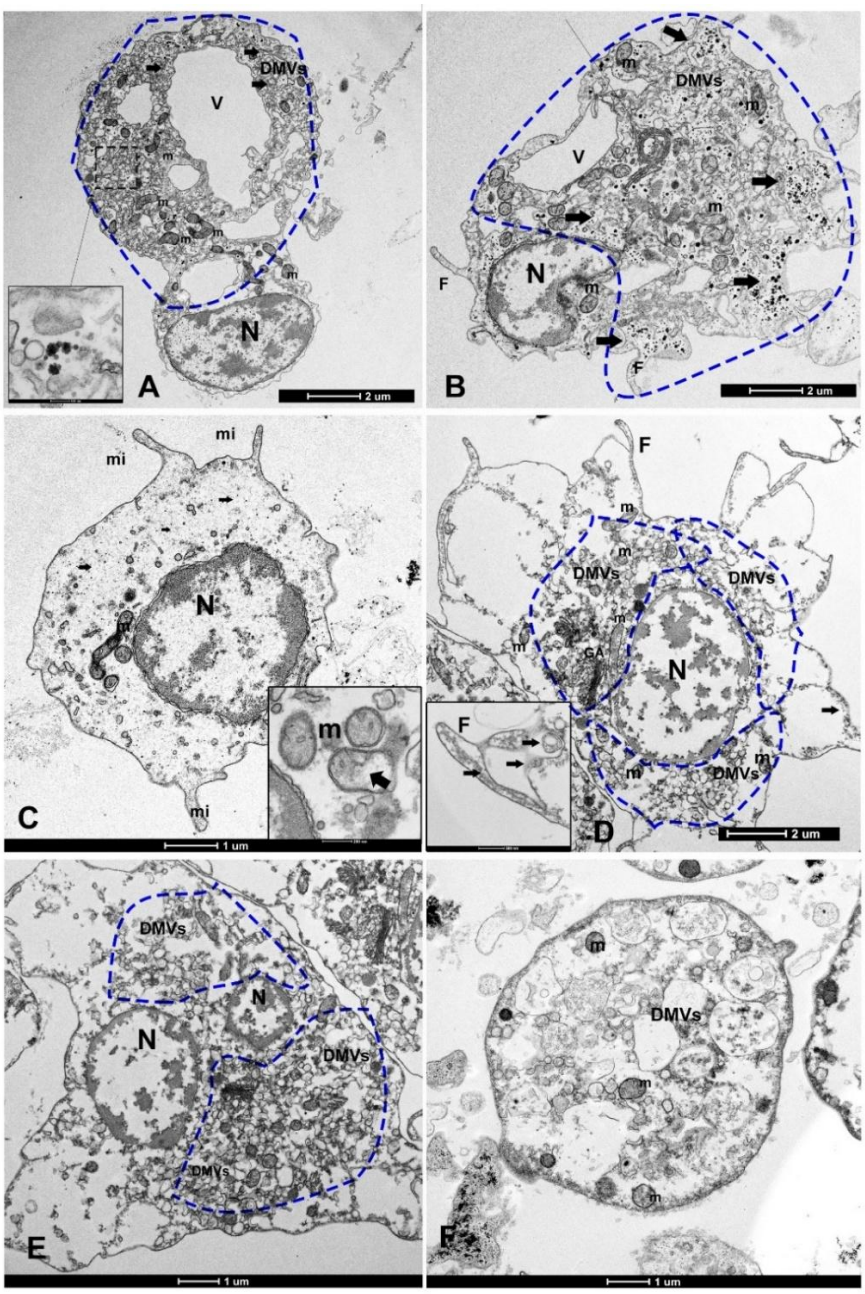


Figure 7. Ultrastructural alterations of *Pinna nobilis* hemocytes in Venice lagoon over the seasons and areas. **In blue dotted lines** the **viral Replication Organelles (vRO**) composed by Double Membrane Vesicles (DMVs). **A.** OA site in May 2024 showed presence of deformed cells displaying large intracellular vacuoles (V) and small forming vesicles containing viral particles in active production represented typically by grouped "flower shaped" structure (inset). **B.** OA site in May 2024 Highly deformed hemocytes displaying large intracellular vacuoles (V), filopodia (F) and small forming vesicles containing forming viral particles (arrows); some virus particles (white arrows) were observed in intracellular vesicles interacting with the

Golgi apparatus (GA) (inset); **C.** CV site in July 2024, some cell displayed absence of cytoskeleton, few small vesicles, scattered viral particles (arrows), mitochondria (m) and intact nucleus (N) and microvilli (mi). **D.** stellate or multipolar cell, developing star-like shapes with multiple projections, often due to cytoskeletal reorganization involving actin tails and microvilli, displayed viral particles at the tips of the filopodia or unassembled amorphic viral material (inset, arrows). **E.** Binucleated hemocyte with small complex DMVs; **D.** dead cell with no visible nucleus and DMVs containing unassembled viral material.

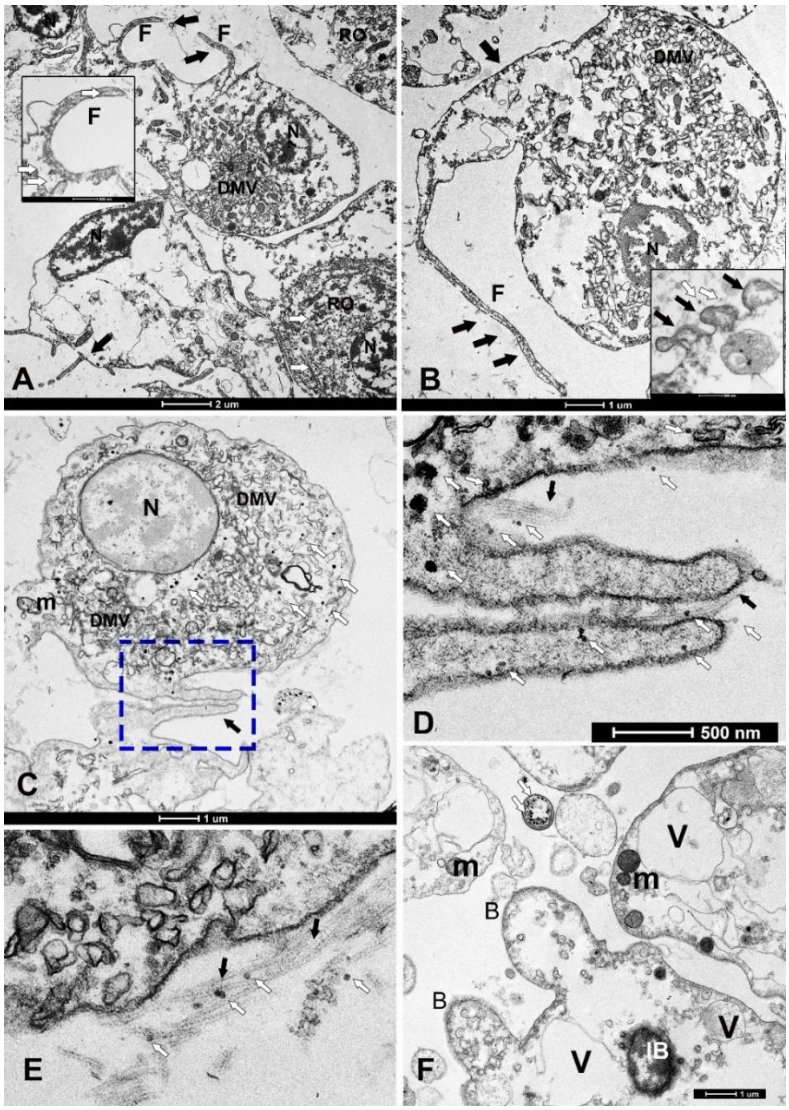


Figure 8. Actin modification during viral replication and egress. A-B. Detail of many infected cells displaying filopodia (black arrow), or buddings (**B**-inset, black arrows), **DMVs**, Replication Organelles (**RO**) and viral particles (white arrows) ;**C-F.** cell-cell contact using filopodia in the blue dotted square (C) and in D and E details of the actin filament (black arrows) and viral particles surfing (white arrows) in the passage

among cells. **F.** Cells formation of budding **(B)** releasing vesicles containing viral particles (white arrows); **IB:** inclusions bodies; **V:** vesicles.

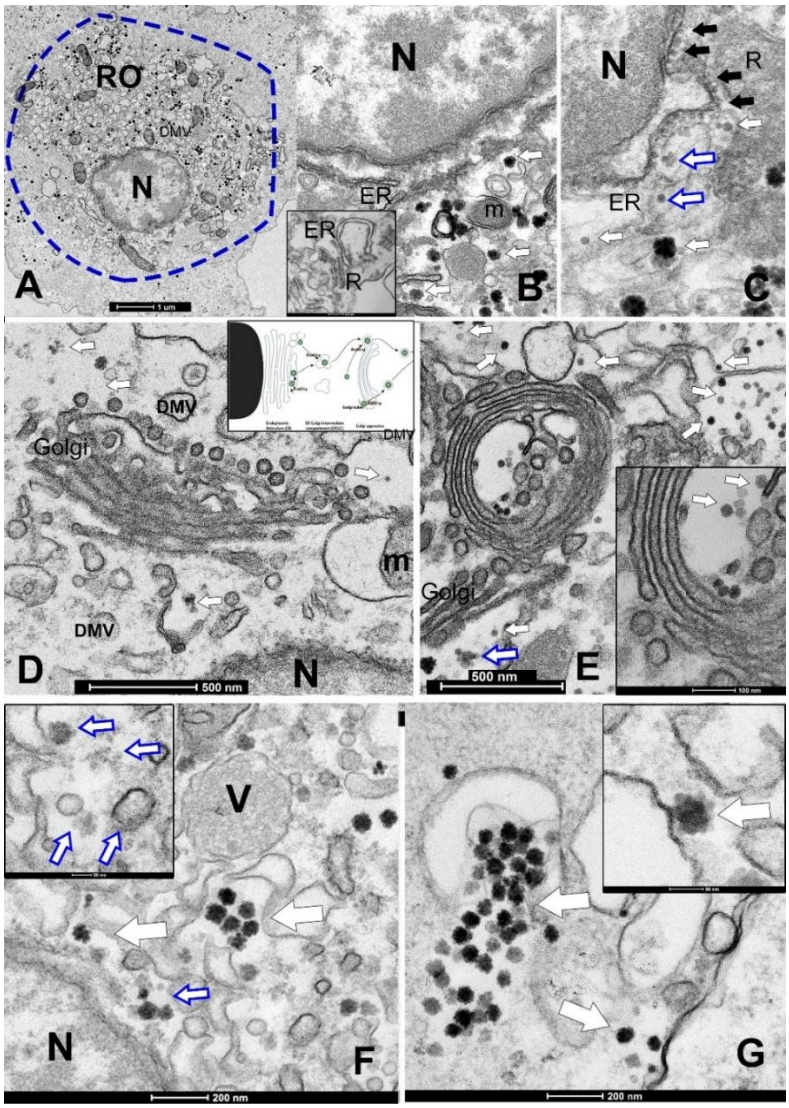


Figure 9. *PnPv* Replication Organelles (RO) derived from the ER. **A.** appearance of the replication organelles organized in the cytoplasm (blu-line circle). **B-C.** Details of ER and ribosomes (**R-black arrows**) in communication with nuclear membrane and presence of forming virions (white arrows); **D-E** Detail of Golgi complex in communication with the ER and used for viral replication (white arrows), with vesicles showing forming not mature viral particles (blue lined arrows) emerging from Golgi Lumen (inset- white arrows). **F-G.** Vesicles in the RO containing the viral material in bigger vesicle (V) and in smaller open

vesicles (**F-inset,** blue lined arrows) also showing the faded not mature viral particles (**blue lined arrows**) and darker grouped rosette-like particles (**G-Inset,** white arrows).

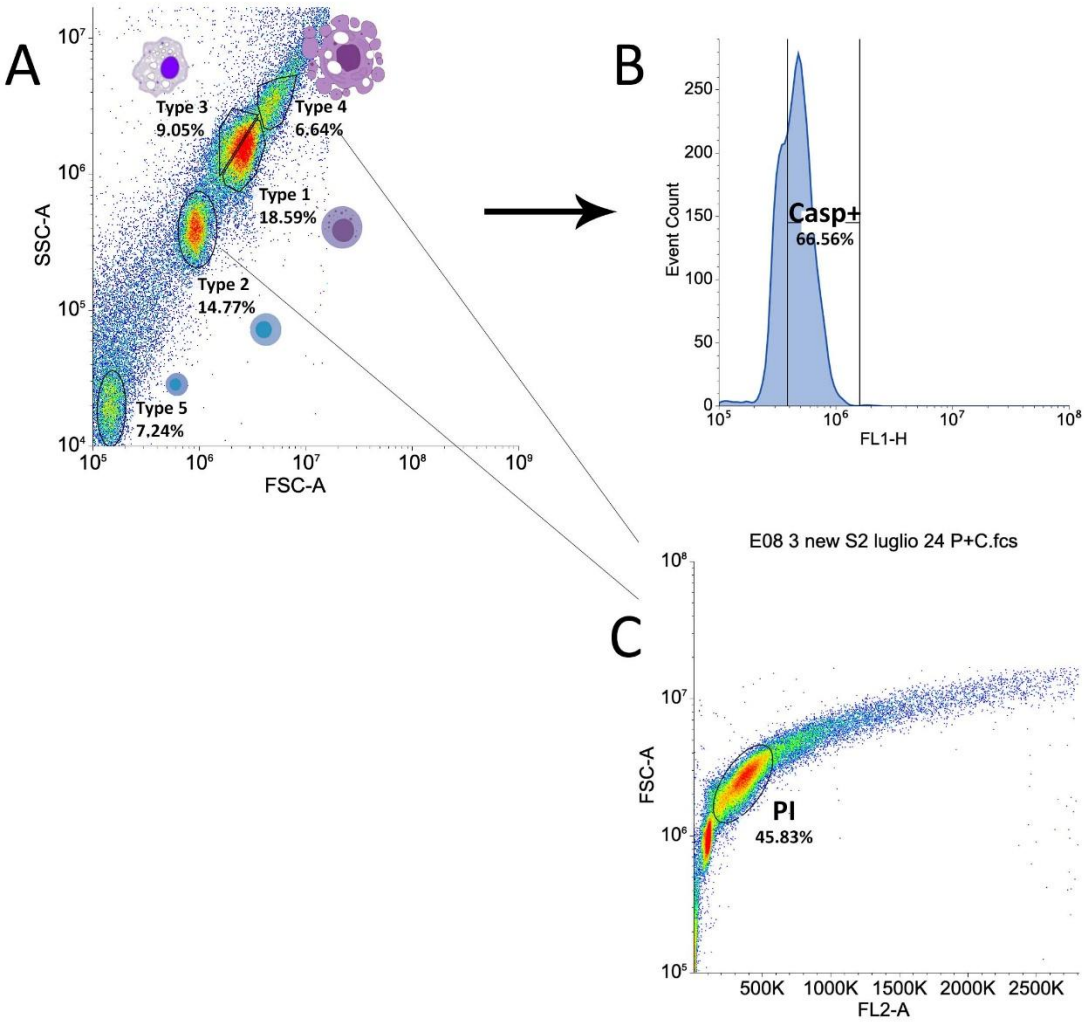


Figure 10. **Cytograms representative of FSC-A/SSC-A dot plot of hemocytes types of *P. nobilis*. A.** Cytology of *P. nobilis* hemocyte populations based on their size and complexity; **B.** histogram of total number cells that express active Caspase-3; **C.** FSC-A/FL2-A dot plot PI positive cells gating strategy.

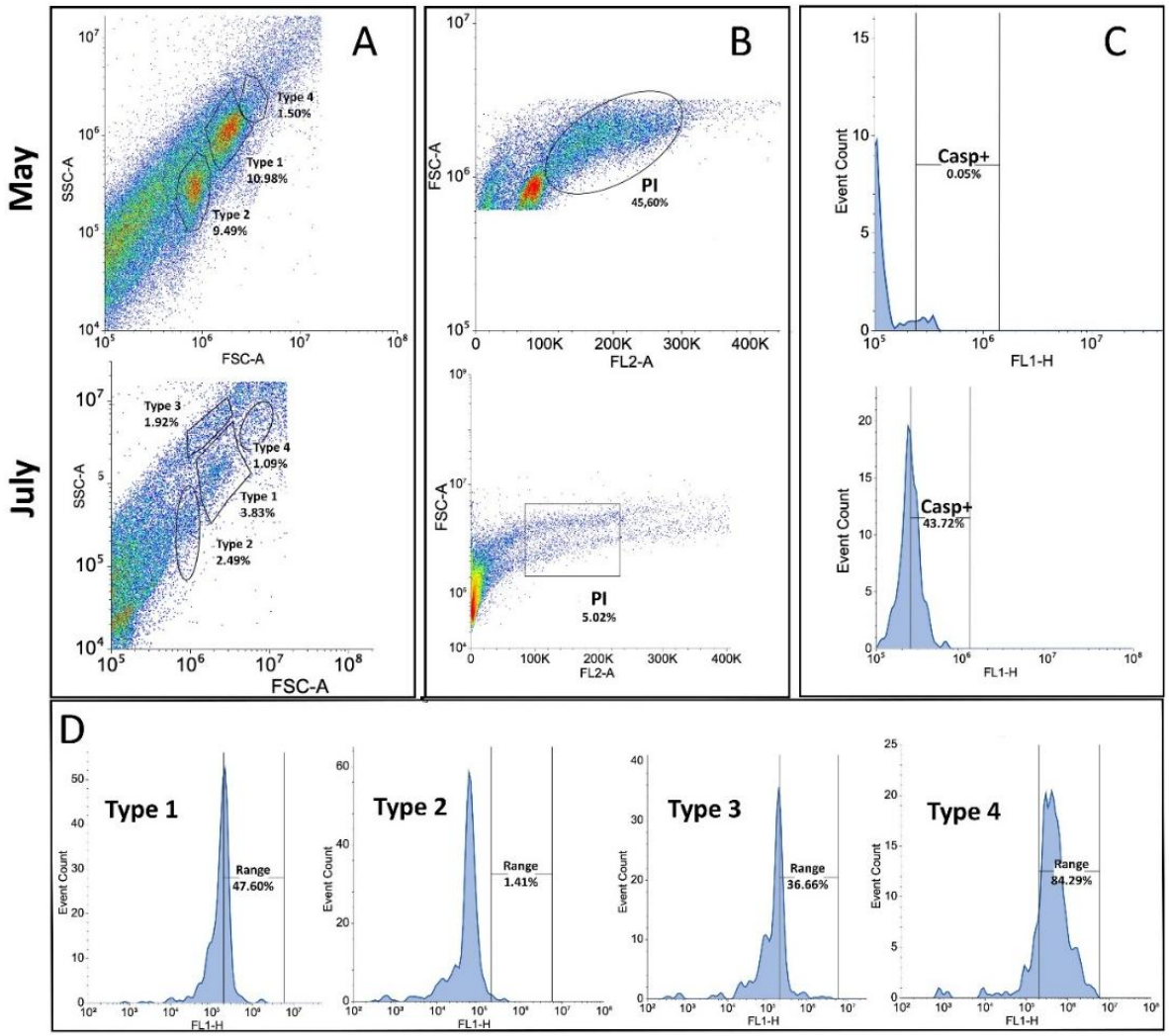


Figure 11. **Cytograms representative FSC-A/SSC-A dot plot of hemocytes of the individual Pn5_OA24 in May and July 2024.** (**A**) linked to cytology of *P. nobilis* hemocyte populations based on their size and complexity, (**B**) FSC-A/FL2-A dot plot PI positive cells gating strategy, (**C**) histogram of total number cells that express active Caspase-3. (**D**) In the panels are shown the percentage of PI positive cells which express active caspase 3 in each sub-populations (from left to right: Type 1, Type 2, Type 3, Type4).

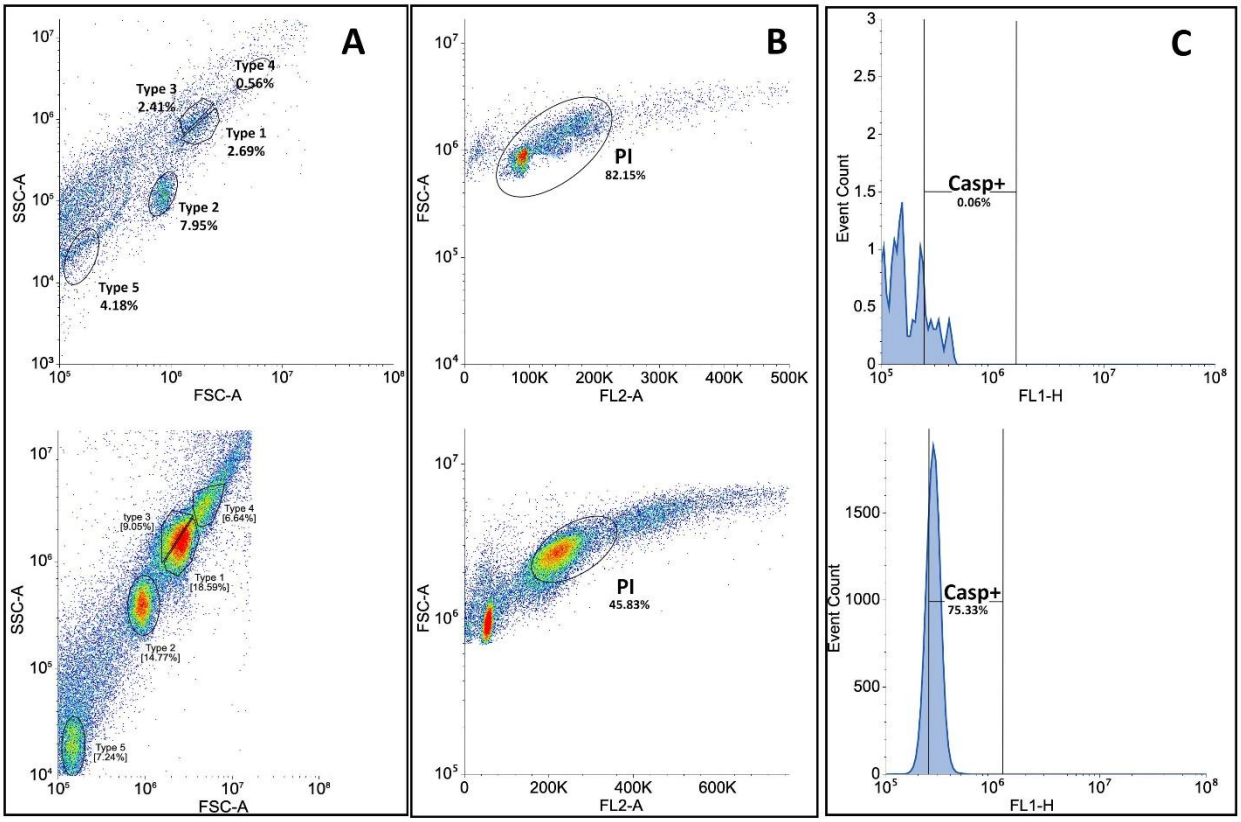


Figure 12. Cytograms representative FSC-A/SSC-A dot plot of hemocytes of the individual Pn3CV24 A. Cytology of hemocyte populations based on their size and complexity; **B.** FSC-A/FL2-A dot plot PI positive cells gating strategy; **C.** histogram of total number cells that express active Caspase-3. In upper panels are shown May samples, in down panel July samples.

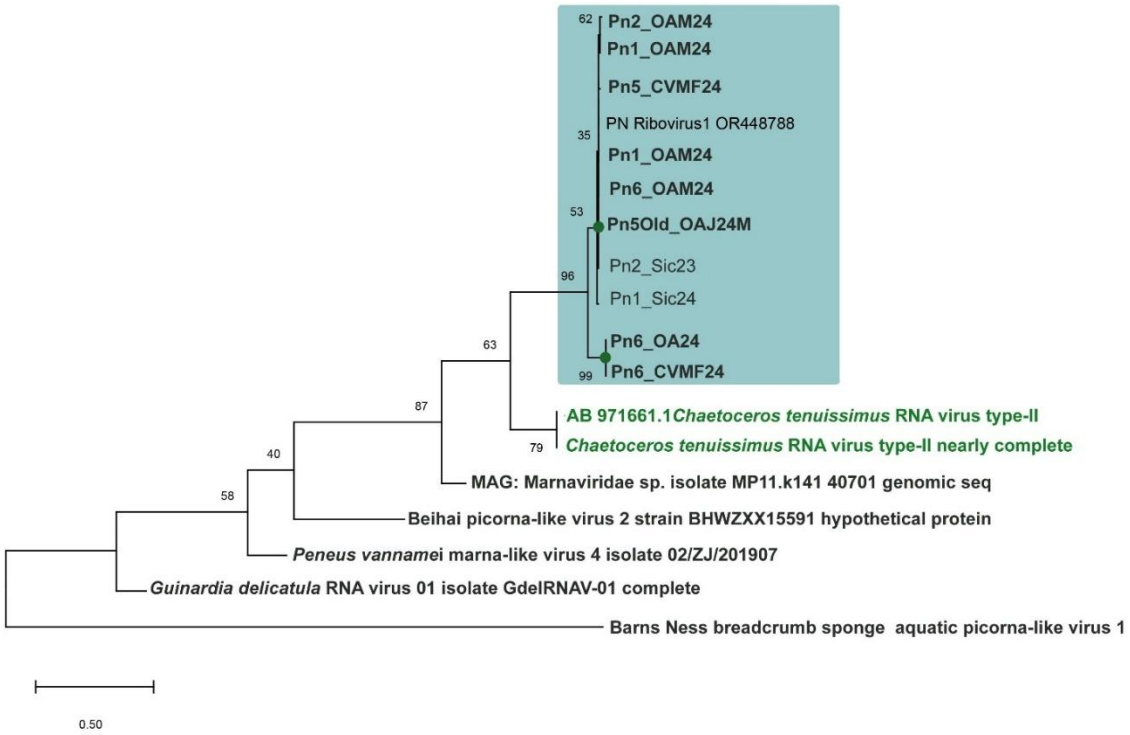
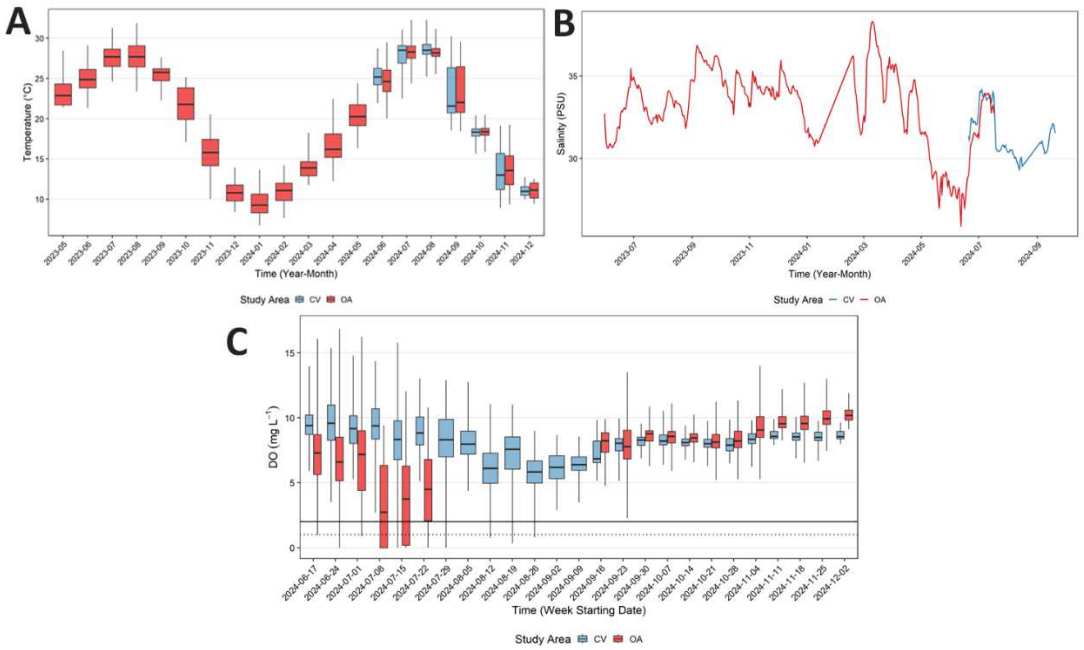


Figure 13. NJ Phylogenetic tree shows the relationship of *PnPv* in Venice Lagoon with other *PnPv* in Sicily and Catalunya and with other Picornavirus of aquatic algae. **In the square in green,** the sequences obtained from the animals in the Venice lagoon.



Supplementary Figure 1 A. Monthly water temperature variability across the two study areas (from May 2023 to December 2024 for OA, and from June to December 2024 for CV). Boxplots show the median, 1st and 3rd quartiles (hinges), and whiskers extending to 2.5 times the interquartile range (IQR) to encompass data variability; individual outliers are omitted for visual clarity. **B.** Daily mean salinity variability across the two study areas (from May 2023 to December 2024 for OA, and from June to December 2024 for CV). **C.** Weekly variability of dissolved oxygen (DO) across the two study areas from June 17 to December 4, 2024. Boxplots show the median, 1st and 3rd quartiles (hinges), and whiskers extending to 2.5 times the interquartile range (IQR); individual outliers are omitted for visual clarity. The continuous line indicates the hypoxic threshold (DO = 2.0 mg L^{-1}), while the dotted line represents the anoxic threshold (DO = 1.0 mg L^{-1}).

	May 2024					**July 2024**					**Health status in October 2024**
sample ID	**Total % Casp 3 Active**	**Type 1 %**	**Type 2%**	**Type 3%**	**Type 4%**	**Total % Casp 3 Active**	**Type 1 %**	**Type 2%**	**Type 3%**	**Type 4%**	
Pn2_OA24	3,34	5,8	8,51	2.96	1,36	0,7	11,84	5,48	6,07	0,4	dead
Pn3_OA24	0,19	7,6	**38,64**	0	1,02	ND	ND	ND	ND	ND	dead
Pn5_OA24	0,07	10,98	9,49	0	1,5	43,72	2,4	2,13	0	0,53	dead
Pn6_OA24	5,08	1,57	1,88	0	0,49	ND	ND	ND	ND	ND	dead
Pn8_OA24	5,68	24,5	4,48	11,27	3,75	ND	ND	ND	ND	ND	dead
Pn1New_OA24	ND	ND	ND	ND	ND	**66,64**	**20,57**	3,47	13,27	3,36	dead
Pn2New_OA24	ND	ND	ND	ND	ND	**59,53**	**30,47**	9,84	16,41	5,19	dead
Pn1_CV24	ND	ND	ND	ND	ND	**28,64**	**13,96**	**16,01**	6,11	4,99	alive
Pn2_CV24	2,77	6,19	7,49	2,64	0,92	ND	ND	ND	ND	ND	alive
Pn3_CV24	0,06	2,96	7,95	2,41	0,56	**75,23**	18,59	14,77	9,05	6,64	alive
Pn4_CV24	0,64	6,24	3,65	0	0	ND	ND	ND	ND	ND	alive
Pn5_CV24	2,4	0	0	0	0	ND	ND	ND	ND	ND	alive
Pn1New_CV24	ND	ND	ND	ND	ND	**36,76**	**28,92**	0,86	13,19	15,63	dead
Pn2New_CV24	ND	ND	ND	ND	ND	0,39	**37,04**	22,1	5,37	5,24	dead
Pn3New_CV24	ND	ND	ND	ND	ND	0,01	**46,52**	14,87	6,88	10,08	alive

Supplementary Table 1. Percentage of active Caspase-3 detected in *P. nobilis* hemocytes in the two areas (OA and CV) **N.D**. not detected. In **bold** the highest percentage of activated caspase-3 is underlined.